The Astrophysical Journal Supplement Series, 257:17 (17pp), 2021 November https://doi.org/10.3847/1538-4365/ac143f

Molecules with ALMA at Planet-forming Scales (MAPS). XVII. Determining the 2D Thermal Structure of the HD 163296 Disk

Jenny K. Calahan[1], Edwin A. Bergin[1], Ke Zhang[1,2,23], Kamber R. Schwarz[3,24], Karin I. Öberg[4], Viviana V. Guzmán[5], Catherine Walsh[6], Yuri Aikawa[7], Felipe Alarcón[8], Sean M. Andrews[4], Jaehan Bae[9,10,24], Jennifer B. Bergner[11,24], Alice S. Booth[6,12], Arthur D. Bosman[1], Gianni Cataldi[7,13], Ian Czekala[14,15,16,17,18,24], Jane Huang[1,4,24], John D. Ilee[6], Charles J. Law[4], Romane Le Gal[4,19,20,21], Feng Long[4], Ryan A. Loomis[22], François Ménard[19], Hideko Nomura[13], Chunhua Qi[4], Richard Teague[4], Merel L. R. van't Hoff[1], David J. Wilner[4], and Yoshihide Yamato[7]

[1] University of Michigan, 323 West Hall, 1085 S. University Ave., Ann Arbor, MI 48109, USA; jcalahan@umich.edu
[2] Department of Astronomy, University of Wisconsin–Madison, 475 N. Charter St., Madison, WI 53706, USA
[3] Lunar and Planetary Laboratory, University of Arizona, 1629 E. University Blvd, Tucson, AZ 85721, USA
[4] Center for Astrophysics | Harvard & Smithsonian, 60 Garden St., Cambridge, MA 02138, USA
[5] Instituto de Astrofísica, Pontificia Universidad Católica de Chile, Av. Vicua Mackenna 4860, 7820436 Macul, Santiago, Chile
[6] School of Physics and Astronomy, University of Leeds, Leeds, LS2 9JT, UK
[7] Department of Astronomy, Graduate School of Science, The University of Tokyo, Tokyo 113-0033, Japan
[8] Department of Astronomy, University of Michigan, 323 West Hall, 1085 S. University Ave., Ann Arbor, MI 48109, USA
[9] Earth and Planets Laboratory, Carnegie Institution for Science, 5241 Broad Branch Road NW, Washington, DC 20015, USA
[10] Department of Astronomy, University of Florida, Gainesville, FL 32611, USA
[11] University of Chicago, Department of the Geophysical Sciences, Chicago, IL 60637, USA
[12] Leiden Observatory, Leiden University, 2300 RA Leiden, The Netherlands
[13] National Astronomical Observatory of Japan, 2-21-1 Osawa, Mitaka, Tokyo 181-8588, Japan
[14] Department of Astronomy and Astrophysics, 525 Davey Laboratory, The Pennsylvania State University, University Park, PA 16802, USA
[15] Center for Exoplanets and Habitable Worlds, 525 Davey Laboratory, The Pennsylvania State University, University Park, PA 16802, USA
[16] Center for Astrostatistics, 525 Davey Laboratory, The Pennsylvania State University, University Park, PA 16802, USA
[17] Institute for Computational & Data Sciences, The Pennsylvania State University, University Park, PA 16802, USA
[18] Department of Astronomy, 501 Campbell Hall, University of California, Berkeley, CA 94720-3411, USA
[19] Univ. Grenoble Alpes, CNRS, IPAG, F-38000 Grenoble, France
[20] IRAP, Université de Toulouse, CNRS, CNES, UT3, 31400 Toulouse, France
[21] IRAM, 300 rue de la piscine, F-38406 Saint-Martin d'Hères, France
[22] National Radio Astronomy Observatory, 520 Edgemont Road, Charlottesville, VA 22903, USA
Received 2021 February 17; revised 2021 July 2; accepted 2021 July 12; published 2021 November 3

Abstract

Understanding the temperature structure of protoplanetary disks is key to interpreting observations, predicting the physical and chemical evolution of the disk, and modeling planet formation processes. In this study, we constrain the two-dimensional thermal structure of the disk around the Herbig Ae star HD 163296. Using the thermochemical code RAC2D, we derive a thermal structure that reproduces spatially resolved Atacama Large Millimeter/submillimeter Array observations (∼0.″12 (13 au)–0.″25 (26 au)) of ^{12}CO $J = 2 - 1$, ^{13}CO $J = 1 - 0$, $2 - 1$, C^{18}O $J = 1 - 0$, $2 - 1$, and C^{17}O $J = 1 - 0$, the HD $J = 1 - 0$ flux upper limit, the spectral energy distribution (SED), and continuum morphology. The final model incorporates both a radial depletion of CO motivated by a timescale shorter than typical CO gas-phase chemistry (0.01 Myr) and an enhanced temperature near the surface layer of the the inner disk ($z/r \geqslant 0.21$). This model agrees with the majority of the empirically derived temperatures and observed emitting surfaces derived from the $J = 2 - 1$ CO observations. We find an upper limit for the disk mass of 0.35 $M_{\odot}$, using the upper limit of the HD $J = 1 - 0$ and $J = 2 - 1$ flux. With our final thermal structure, we explore the impact that gaps have on the temperature structure constrained by observations of the resolved gaps. Adding a large gap in the gas and small dust additionally increases gas temperature in the gap by only 5%–10%. This paper is part of the MAPS special issue of the Astrophysical Journal Supplement.

Unified Astronomy Thesaurus concepts: Protoplanetary disks (1300); Astrochemistry (75)

Supporting material: figure set

1. Introduction

The two-dimensional (radial + vertical) thermal structure of protoplanetary disks has been a long sought-after property due to its importance in interpreting of observations and its importance for disk evolution. Disk temperature sets the physical and chemical evolution of disk material, with subsequent implications for planet formation. The translation of observations into fundamental disk properties, namely gas mass, strongly depends on the assumed underlying disk temperature at which the observed molecule emits. The mass tracer HD (Bergin et al. 2013; McClure et al. 2016; Bergin & Williams 2017; Trapman et al. 2017; Kama et al. 2020) especially requires a well-defined disk thermal structure as its $J = 1 - 0$ transition has an E_{up} of 128.5 K. This approaches typical temperatures within the warm molecular layer of protoplanetary disks. The temperature throughout the disk regulates physical evolution by setting local sound speeds (Bergin & Williams 2017), turbulent viscosity

[23] NASA Hubble Fellow.
[24] NASA Hubble Fellowship Program Sagan Fellow.

(Shakura & Sunyaev 1973; Penna et al. 2013), and vertical flaring of the disk (Kenyon & Hartmann 1987), which can in turn set the angle of incidence of stellar irradiation, further changing the thermal structure. From a chemical perspective, gas temperature controls the rate of gas-phase exothermic reactions. Temperature also dictates the rates of gas-phase deposition and thermal sublimation, effectively prescribing the relative radial chemical composition of ices in the midplane. These sublimation fronts, or snowlines, have been theorized to be favorable sites for planet formation (Hayashi 1981; Stevenson & Lunine 1988; Zhang et al. 2015; Schoonenberg & Ormel 2017), and may affect the chemical composition of a planetary embryo or accreting atmosphere (e.g., C/O; Öberg et al. 2011; Öberg & Bergin 2016; Cridland et al. 2020).

The most robust attempts to uncover the temperature profile of protoplanetary disks involve a convergence of observations of multiple gas emission lines and thermochemical modeling (e.g Kama et al. 2016; Woitke et al. 2019; Rab et al. 2020; Calahan et al. 2021). With the advent of the Atacama Large Millimeter/submillimeter Array (ALMA), spatially resolved observations of disks became feasible, providing the first empirical measurements of the radial distribution of dust and gas at high angular resolution. This gave much-needed constraints for protoplanetary disk models. The commonly observed ^{12}CO $J = 2 - 1$ is optically thick in most gas-rich disks due to it being the second most abundant molecule in the gas phase after H_2. Lower-energy transitions and less-abundant isotopologues emit from lower vertical layers, resulting in intensity profiles that are affected by temperature and CO surface density/abundance where that species is emitting. Thus, joint modeling of multiple spatially resolved CO isotopologues provides radial and vertical constraints on the temperature and CO chemistry.

This study determines the 2D temperature structure of the disk around HD 163296, as part of the ALMA-MAPS project, which observed five protoplanetary disks at high resolution. Each disk is detailed in Öberg et al. (2021). HD 163296 is a Herbig Ae star with a stellar mass of 2.0 $M_\odot$ (Andrews et al. 2018; Wichittanakom et al. 2020) surrounded by a massive disk (8×10^{-3} –5.8×10^{-1} $M_\odot$; Kama et al. 2020, and references therein) 101 pc away (Bailer-Jones et al. 2018; Gaia Collaboration et al. 2018). Both millimeter continuum and scattered-light observations show a significant substructure (Grady et al. 2000; Wisniewski et al. 2008; Benisty et al. 2010; Garufi et al. 2014; Monnier et al. 2017; Muro-Arena et al. 2018; Isella et al. 2018; Dent et al. 2019; Rich et al. 2020) including three gaps in millimeter continuum observations at 10, 48, and 86 au. These gaps have been prime targets to test planet formation theories; planets ranging in mass from 0.07–4.45 M_J have been theorized to exist within the gaps in HD 163296 (Zhang et al. 2018). The temperature of both the gas and dust populations in the gaps can be used to directly inform planet formation models. Kinematic studies of HD 163296 suggest the existence of a $\sim$2 M_J planet at 260 au (Pinte et al. 2018, 2020). Further analysis of the velocity structure by Teague et al. (2019) mapped out the 3D gradient of velocity using ^{12}CO $J = 2 - 1$ from the DSHARP project (Andrews et al. 2018), and in Teague et al. (2021). Meridional flows are found at the location of the continuum gaps, indicative of ongoing planet formation. The protoplanetary disk around HD 163296 presents an excellent case for determining the 2D thermal profile using some of the highest resolution data available for a disk in which planets are believed to be actively forming.

Two-dimensional temperature structures for HD 163296 have been modeled previously using a combination of spatially unresolved observations of the CO rotational ladder, and other higher-energy molecular and atomic transitions (Qi et al. 2011; de Gregorio-Monsalvo et al. 2013; Rosenfeld et al. 2013) with a few studies utilizing thermochemical modeling to match numerous observations (Tilling et al. 2012; Fedele et al. 2016; Woitke et al. 2019). These studies found that HD 163296 is a relatively cooler disk compared to other disks surrounding Herbig stars. Resolved observations of ^{12}CO $J = 2 - 1$ have also revealed insight into the temperature within the disk gaps (Rab et al. 2020).

The observations from the ALMA-MAPS program consist of highly resolved ($\sim$0.″12–0.″25), and high signal-to-noise ratio observations of ^{12}CO $J = 2 - 1$, ^{13}CO $J = 2 - 1$, $1 - 0$, C^{18}O $J = 2 - 1$, $1 - 0$, and C^{17}O $J = 1 - 0$. These observations show structure in the radial intensity profiles (Law et al. 2021a) and CO column density (Zhang et al. 2021; hereafter Z21) and allow for a new derivation of the 2D thermal structure.

This paper is organized as follows: We detail our modeling procedure and describe the observations in Section 2. In Section 3, we present our best-fit thermal model and the necessary alterations needed to fit each observed line. In Section 4, comparisons of the final model to the empirically derived temperature structure and emitting surfaces are discussed along with our derivation of an upper mass limit for the HD 163296 disk and we explore CO/H_2 degeneracy and temperature effects within the two largest gaps of the HD 163296 disk. We summarize our findings in Section 5.

2. Methods and Observations

2.1. Observations

We use observations of ^{12}CO $J = 2 - 1$, C^{18}O $J = 2 - 1$, $1 - 0$, ^{13}CO $J = 2 - 1$, $1 - 0$, and C^{17}O $J = 1 - 0$ toward the HD 163296 disk. For this study, we use images which have an average spatial resolution of 26 au for the $1 - 0$ transitions (0.″25) and 13 au for the $2 - 1$ transitions (Öberg et al. 2021, and Table 1). The final image cubes used for this study had a spectral resolution of 200 m s^{-1}, and used a robust = 0.5 weighting. The robust = 0.5 images were used as they provided the highest absolute resolution. These images were "JvM corrected" (Jorsater & van Moorsel 1995), which refers to the method of scaling the residuals in the image cube to have identical units to the CLEAN model. This ensures that the final image used for moment zero maps, and subsequent radial profiles, have the correct units (Jy CLEAN beam^{-1}); see Czekala et al. (2021) for a detailed explanation. The MAPS program summary, along with data reduction and calibration specifics can be found in Öberg et al. (2021), and the methods of the imaging process are thoroughly described in Czekala et al. (2021). Radial intensity profiles are created for each CO line for comparison with our model results. Radial profile derivations are presented in Law et al. (2021a). The package BETTERMOMENTS[25] (Teague & Foreman-Mackey 2018) is used to extract the moment zero map which is then used to calculate the radial intensity profile using GOFISH[26] (Teague 2019). We follow the same methods in creating our simulated radial intensity profiles.

In addition to ALMA observations of CO, we also compared our model to the Herschel Space Observatory observation of HD

[25] https://github.com/richteague/bettermoments
[26] https://github.com/richteague/gofish

Table 1
ALMA Observations Summary

Transition	Frequency (GHz)	E_{up} (K)	Beam ($'' \times ''$)	PA (deg)	rms (mJy beam^{-1})
^{12}CO $J = 2 - 1$	230.538	16.6	0.14×0.10	−76.3	0.561
^{13}CO $J = 1 - 0$	110.201	5.3	0.28×0.22	−89.1	0.434
^{13}CO $J = 2 - 1$	220.399	15.8	0.14×0.11	−76.6	0.541
C^{18}O $J = 1 - 0$	109.782	5.3	0.28×0.22	−88.8	0.449
C^{18}O $J = 2 - 1$	219.560	15.8	0.14×0.11	−76.5	0.385
C^{17}O $J = 1 - 0$	112.359	5.4	0.28×0.21	−89.5	0.528

Note. These data were taken from values in Öberg et al. (2021) and Czekala et al. (2021), where details regarding the data reduction can also be found.

$J = 1 - 0$ and $2 - 1$ toward HD 163296. The HD observations were made using the Photoconductor Array Camera and Spectrometer (PACS) instrument and were spatially and spectral unresolved. Kama et al. (2020) used archival data from the DIGIT program (PI N. J. Evans) to determine the upper flux limits for 15 Herbig Ae/Be disks, including HD 163296. They found an upper limit for the flux of the $J = 1 - 0$ line of $\leqslant 0.9 \times 10^{-17}$ W m^{-2} and for the $J = 2 - 1$ they determined a flux of $\leqslant 2.4 \times 10^{-17}$ W m^{-2}.

2.2. RAC2D Physical Structure

In this study, we use the time-dependent thermochemical code RAC2D[27] (Du & Bergin 2014) to model the thermal structure of the HD 163296 disk, and create simulated observations to compare with the ALMA data. A brief description of the physical code of RAC2D is given below; a detailed description of the code can be found in the aforementioned paper.

RAC2D takes into account both the disk gas and dust structure while simultaneously computing the temperature and chemical structure over time. Our model consists of three mass components: gas, small-dust ($\leqslant$ micrometer), and large-dust grains ($\leqslant$ millimeter). The distribution of each component is described by a global surface density distribution (Lynden-Bell & Pringle 1974), which is widely used in the modeling of protoplanetary disks and corresponds to the self-similar solution of a viscously evolved disk.

$$\Sigma(r) = \Sigma_c \left(\frac{r}{r_c}\right)^{-\gamma} \exp\left[-\left(\frac{r}{r_c}\right)^{2-\gamma}\right], \quad (1)$$

r_c is the characteristic radius at which the surface density is Σ_c/e and γ is the power-law index that describes the radial behavior of the surface density.

A density profile for the gas and dust components can be derived from the surface density profile and a scale height:

$$\rho(r, z) = \frac{\Sigma(r)}{\sqrt{2\pi}\, h(r)} \exp\left[-\frac{1}{2}\left(\frac{z}{h(r)}\right)^2\right], \quad (2)$$

$$h = h_c \left(\frac{r}{r_c}\right)^{\Psi}, \quad (3)$$

where h_c is the scale height at the characteristic radius, and Ψ is a power index that characterizes the flaring of the disk structure.

Both dust populations follow a Mathis–Rumpl–Nordsieck grain distribution $n(a) \propto a^{-3.5}$ (Mathis et al. 1977). The small-dust grains have radii between 5×10^{-3}–1 μm, and the large grains have radii between 5×10^{-3}–10^3 μm. The following description of the dust-grain population used in this study is adopted from Z21, which used both the HD 163296 spectral energy distribution (SED) and millimeter continuum observations to constrain the dust population. The gas and small-dust grains are spatially coupled and extend to 600 au. The large-dust population is settled in the midplane with a smaller vertical extent ($h = 1.69$ au) and radial extent (240 au). This settled large-grain population is the result of dust evolution, namely vertical settling to the midplane and radial drift. The large-grain population has a unique, nonsmooth, surface density profile that reproduces the millimeter continuum observations of the HD 163296 disk (Z21). The dust composition adopted is consistent across the MAPS Collaboration, and opacity values are calculated based on Birnstiel et al. (2018). Large dust grains consist of water ice (Warren & Brandt 2008), silicates (Draine 2003), troilites, and refractory organics (Henning & Stognienko 1996). Small-dust grains consist of 50% silicates and 50% refractory organics.

2.3. RAC2D Dust and Gas Temperature

The code computes a dust and gas temperature after initializing RAC2D with a model density structure for each population, a stellar spectrum, and external UV radiation field ($G_0 = 1$). The stellar spectrum we use is a composite of multiple UV and X-ray observations, and is further detailed in Z21. The determination of dust and gas temperature is an iterative process that is allowed to change over time due to the evolving chemical composition. The dust thermal structure is calculated first using a Monte Carlo method to simulate photo absorption and scattering events. This also results in a radiation field spanning from centimeter to X-ray wavelengths.

We adopt the reaction rates from the UMIST 2006 database (Woodall et al. 2007) for the gas-phase chemistry with additional rates considering the self-shielding of CO, H_2, H_2O, and OH, dust-grain surface chemistry driven by temperature, UV, cosmic rays, and two-body chemical reactions on dust-grain surfaces (see references given by Du & Bergin 2014). Chemical processes also provide heating or cooling to the surrounding gas. These mechanisms, along with stellar and interstellar radiation, drive the thermal gas structure. Our study explores models that account for 0.01 Myr of chemical evolution. This is a relatively short period of time compared to disk lifetimes and is motivated by an average CO-processing timescale, which is found to be on the order of 1 Myr (Bergin et al. 2014; Bosman et al. 2018; Schwarz et al. 2018). The calculated depletion profile of CO is motivated by observations, and thus accounts for any long-timescale chemical effects that have taken place in the disk's history; we

[27] https://github.com/fjdu/rac-2d

did not want to further process CO by running the disk model for longer than 0.01 Myr. It is also worth noting that the exact timescale will not affect our final temperature structure nor CO column density distribution; it will only affect the CO depletion profile. CO will be created or destroyed in our chemical network over time, and the CO depletion profile acts to counter any over- or underabundance of CO being produced. While localized variations in the CO abundance may affect the gas temperature, the global temperature structure is not strongly affected by the CO abundance. Finally, at the end of a given run, we extracted the dust and gas thermal profiles.

Simulated line images for CO, ^{13}CO, C^{18}O, C^{17}O, and HD are necessary for our comparison to observations. We did not model isotopologue fractionation in this chemical network, as fractionation of CO is not significant in a massive disk like HD 163296 (Miotello et al. 2014). Thus, we computed ^{13}CO and C^{18}O abundances based on interstellar medium ratios of ^{12}CO/^{13}CO = 69, ^{12}CO/C^{18}O = 557, C^{18}O/C^{17}O = 3.6 (Wilson 1999). Given these abundances and the local gas temperature, RAC2D computes synthetic channel maps using a ray-tracing technique. We then convolved these simulated observations with the corresponding ALMA CLEAN beam to make direct comparisons to data. To directly compare to observations, we created simulated integrated radial intensity profiles of each of the CO lines, following the methods from Law et al. (2021a). Our simulated observations have the same beam sizes, spectral resolution, and pixel size as what is reported in Öberg et al. (2021). To recreate the unresolved integrated flux measurements for HD, we convolved our model HD lines with a Gaussian profile corresponding to the velocity resolution of the Herschel PACS instrument: $\sim$300 km s^{-1} at $\sim$112 μm and $\sim$100 km s^{-1} at $\sim$51 μm (Poglitsch et al. 2010).

We began with a model of the HD 163296 disk from Z21, which starts with an initial set of disk parameters taken from the literature (see references within Zhang et al. 2021) and applied the observed UV, X-ray, and photosphere stellar spectra. These authors then determined a gas and dust density and dust temperature structure by matching the SED and ALMA continuum image using RADMC3D (Dullemond et al. 2012). Given this initial density and dust temperature distribution, RAC2D is then used to compute the gas temperature and disk chemistry. Z21 found that in order for the simulated radial profiles to match what is observed, they must modify the CO abundance relative to H_2 as a function of radius. They use the difference between C^{18}O $J = 2 - 1$ as observed and as simulated to predict a CO depletion profile. That depletion profile is shown in Figure 1. The initial chemical abundances used in Z21 are shown in Table 2 and final model parameters are summarized in Table 3. In the study described here, we use the Z21 model as a starting point to derive a 2D temperature map incorporating additional constraints from CO isotopologues, multiple higher-level CO transitions, and HD flux. We note that while any revisions made were important to constrain the disk temperature structure, they do not affect the results reported in Z21, and the final CO column densities from this model agree well with what is found in Z21.

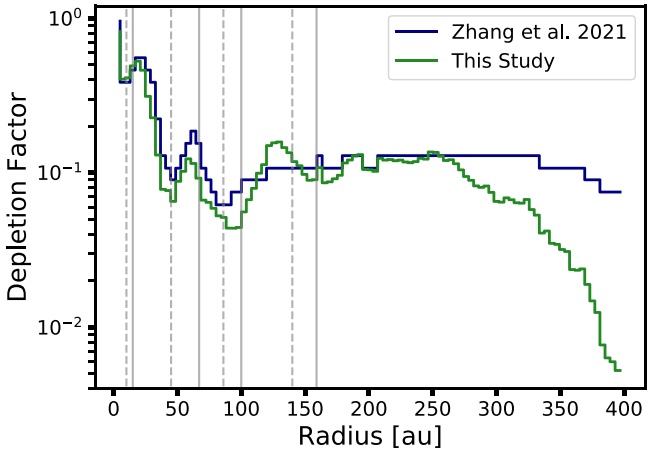

Figure 1. Multiplicative depletion factor for the initial CO abundance (CO/H = 1.4×10^{-4}) as shown in Table 2. Light gray lines indicate the location of the dust rings (solid) and gaps (dashed). The line in blue shows the CO depletion as derived by Z21 and is determined after an initial thermochemical model of the HD 163296 disk and is based on the C^{18}O $J = 2 - 1$ observation, and acts as a starting point for our CO depletion determination. The green line represents the final CO depletion, also motivated by the C^{18}O $J = 2 - 1$ flux, but it is taken into account at the beginning of the chemical and thermal calculations.

Table 2
Initial Chemical Abundances for Final Model

	Abundance Relative to Total Hydrogen Nuclei
H_2	5×10^{-1}
HD	2×10^{-5}
He	0.09
CO[a]	See Figure 1
N	7.5×10^{-5}
H_2O (ice)	1.8×10^{-4}
S	8×10^{-8}
Si^+	8×10^{-9}
Na^+	2×10^{-8}
Mg^+	7×10^{-9}
Fe^+	3×10^{-9}
P	3×10^{-9}
F	2×10^{-8}
Cl	4×10^{-9}

Note.
[a] CO starts with an abundance of 1.4×10^{-4} with an imposed radial depletion profile as shown in Figure 1.

3. Results

3.1. CO Depletion

In Z21, depletion of CO was calculated based on a model of the disk based on previous determinations of disk parameters and the C^{18}O $J = 2 - 1$ radial intensity profile. The CO was depleted throughout the disk at the start of the ray-tracing method that creates the simulated observations, i.e., after the temperature and chemical evolution of the disk. This depletion means the CO abundance is reduced from its expected value ($\sim 10^{-4}$ relative to H_2) in layers where the dust temperature is above the CO sublimation point and the gas is self-shielded from radiation. Since CO is a significant coolant in the disk-surface layers where the dust and gas are thermally decoupled, any depletion of CO may affect the thermal structure. Thus, for this study, we recalculated the CO depletion factors. We started by applying the Z21 CO depletion to the initial CO abundance. After running the model for 0.01 Myr, there were small inconsistencies between the simulated and observed C^{18}O $J = 2 - 1$ radial emission profiles (see Figure A1). We then calculated a new CO depletion profile by determining what

Table 3
Gas and Dust Population Parameters: Best-fit Model Values

	Gas	Small Dust	Large Dust
Mass ($M_\odot$)	0.14	2.6×10^{-4}	2.4×10^{-3}
Ψ	1.08	1.08	1.08
γ	0.8	0.8	0.1
h_c (au)	14.5	14.5	...
r_c (au)	165	165	...
r_{in} (au)	0.45	0.45	0.45
r_{out} (au)	600	600	240

Note. Final values of the HD 163296 model that reproduces the CO, HD, and SED observations. Small dust-grain sizes range from 5×10^{-3}–1 μm, large dust-grain sizes range from 5×10^{-3}–1×10^{3} μm. The large-dust population does not have associated h_c nor r_c because the surface density is set by continuum observations, thus it is nonsmooth and not dictated by Equations (1)–(3).

factor of increase or decrease in CO flux would be needed to reproduce the observation at each radii (using the same radial resolution as Z21). That factor was then applied to the original CO depletion profile at the corresponding radius. The model was then run again with the new CO depletion profile. We needed to iterate this process three times, and stopped iterating once the χ^2 value (using `stat.chisquare` function from the `scipy` package and comparing the simulated and observed $C^{18}O$ $J = 2 - 1$ radial profile intensity values) had dropped well below that of the first attempts. The first three attempts had a χ^2 value of 8.06–9.72, and the final model $\chi^2 = 2.47$. The final depletion profile is shown in Figure 1, and on average the newly calculated CO depletion is 33% more depleted than that derived in Z21. Most of the difference is at large radii where the profiles vary by only 16% within 200 au.

There is a strong decrease in CO abundance beyond ~250 au, which is not seen in the CO depletion profile calculated by Z21. The CO depletion profile from Z21 accounts for an initial CO depletion in HD 163296 plus 1 Myr of CO processing accounted for in the RAC2D chemical evolution. In our model, we include only 0.01 Myr of additional chemical processing, thus we do not attempt to model the full evolution of CO. In the Z21 model, their derived CO depletion profile takes into account chemical processing that occurs over the course of 1 Myr. The difference in CO abundance for our HD 163296 disk model as compared to the Z21 model is then attributed to chemical CO depletion mechanisms that occur over 1 Myr. In the Z21 model, fully self-shielded CO becomes frozen out and interacts with OH that is frozen out onto grains and creates CO_2. In our model, we treat past CO chemistry as an initial condition. We find it necessary to additionally deplete CO beyond ~240 au in the model that runs for only 0.01 Myr, since the pathway to convert CO and CO_2 is unavailable within that time.

3.2. Additional Heating

While our initial model with the updated CO depletion profile reproduced most of the observed CO lines, ^{12}CO $J = 2 - 1$ was underpredicted on average by a factor of 1.6 within 100 au, and a factor of 2.2 within 35 au. We completed a thorough exploration of the parameter space including gas mass, small-dust mass, surface density power-law index (γ), flaring index (Ψ), scale height (h_c), critical radius (r_c), and outer radius (see Appendix A). However, we found no combination of parameters that could improve the ^{12}CO $J = 2 - 1$ flux agreement while leaving the other lines consistent with observations. This result, together with the high optical depth of the ^{12}CO $J = 2 - 1$ transition, suggests that the discrepancy is due to a higher temperature in the CO-emitting layer. This has also been seen in de Gregorio-Monsalvo et al. (2013); ^{12}CO $J = 3 - 2$ was observed to be brighter than their model, which matches the outer disk. To solve this issue they increased the gas temperature beyond the dust temperature within 80 au in their HD 163296 disk model.

This higher gas temperature requires additional heating, beyond the level generated by the UV and X-ray field in our model. We began by isolating the layers in which the gas and dust thermal structure are decoupled. Within those regions, with the goal of representing excess heating due to radiation from the star, we artificially increased the gas temperature after the thermochemical calculation, and simulated new CO observations. We increased the temperature in this region following a power law dependent on radius, and by a constant amount vertically (see the equation below). There was no realistic amount of heating within the decoupled layer that would increase the intensity of the ^{12}CO $J = 2 - 1$ line to match what is observed; any excess heating only affected emission from the inner few astronomical units. This then suggests that the ^{12}CO $J = 2 - 1$ primarily emits from the region lower in the disk, in which the dust and gas temperatures are coupled, and the necessary excess heating would decouple the gas and dust temperatures.

We increase the gas temperature radially following the dust thermal profile. Increasing the gas temperature as function of radius following a power law,

$$T_{\rm new} = T_{\rm original} \times \left(\frac{r}{100\ {\rm au}}\right)^{-0.4}$$

above a constant ratio of height over radius $(z/r) = 0.21$ reproduces the observed ^{12}CO $J = 2 - 1$ radial profile. Outside of this region, the gas and dust temperatures remain coupled. Various z/r limits were explored, and $z/r = 0.21$ produced a result that appeared to significantly affect the ^{12}CO $J = 2 - 1$ line while not altering any other lines (see Figure 2 for a sample of the parameter exploration results). It can then be presumed that the emitting surface of ^{12}CO $J = 2 - 1$ exists at or above $z/r = 0.21$ within 100 au, and all other lines emit from below these heights (this is supported by further analysis probing the emitting surfaces of each $2 - 1$ transition, see Section 4.1 and Law et al. (2021b)). Higher transitions of CO, up to ^{12}CO $J = 23 - 22$ have been observed using the SPIRE instrument on Herschel and are compiled in Fedele et al. (2016). These transitions will primarily emit from the very inner regions of the disk, and would be affected by the increase in temperature. Our final model reproduces all of the observed fluxes of the 19 higher-level transitions of CO, most within 1σ uncertainly, and five of the transitions fit within 2σ or 3σ uncertainty (see Table B1). While the flux predictions from the model all fall within 3σ, all are on the fainter end of the observed flux. Additionally, the HD $J = 2 - 1$ flux does not change significantly, increasing only by 7%, remaining well below the observed upper limit. A model without the additional heat produces a CO flux from the $J = 11 - 10$ transition that is more than twice as small as our final model. On average, for the transitions between $J = 11 - 10$ and $J = 23 - 22$, a model

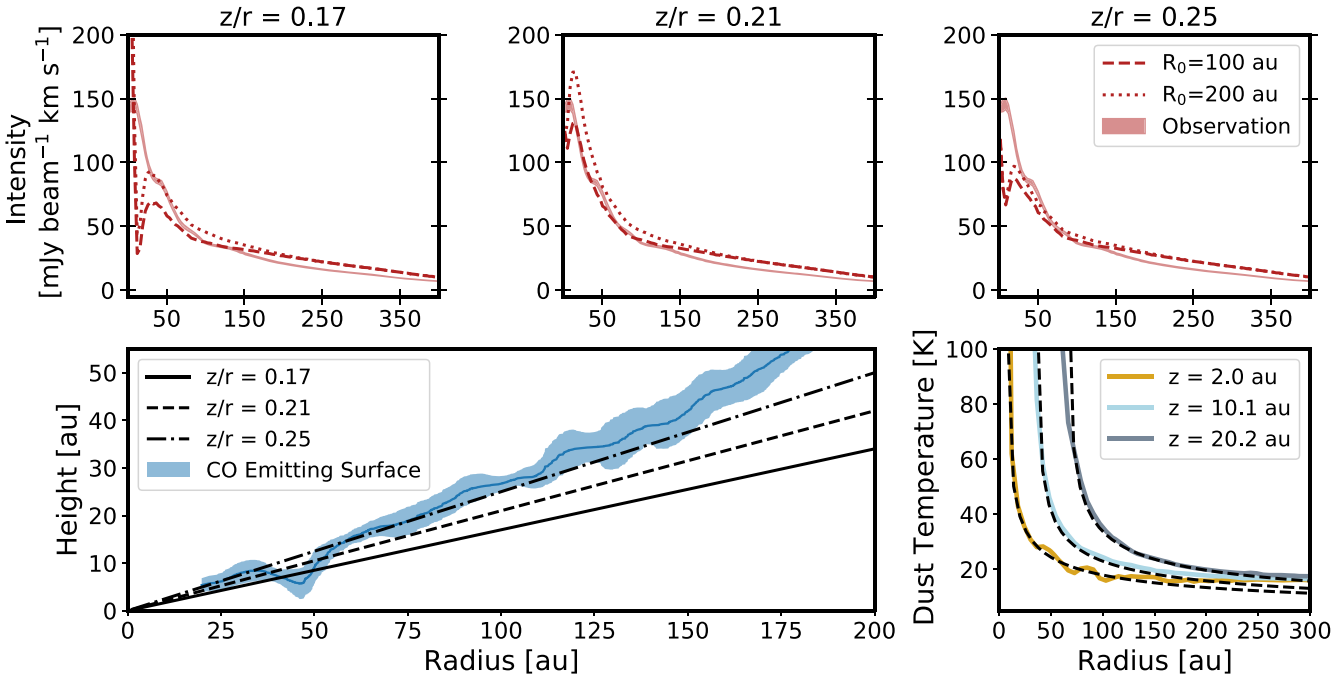

Figure 2. These figures represent the effect of excess heating on the ^{12}CO $J = 2 - 1$ line profile given different height over radius (z/r) limits (0.17, 0.21, 0.25, columns) and R values (100 and 200 au, dashed line and dotted line) using $(r/R_0)^{-0.4}$ to calculate the excess factor of heat in the regions above a certain z/r. We sought to find a z/r and R_0 value that would reproduce the observed ^{12}CO $J = 2 - 1$ radial profile (solid red lines). The above is just a sample of the z/r and R_0 values explored, with our final model using a z/r limit of 0.21 and $R_0 = 100$ au. The bottom left plot shows the observed emitting surface of ^{12}CO $J = 2 - 1$ (blue) and the z/r values explored. The bottom right plot shows the dust temperature over radius at different heights in the disk, which follow an inverse power-law function, and each dashed black line is a power law following $r^{-0.4}$, which is what we use to determine the excess heat factor.

without the additional heat produces a CO flux over four times lower than our current model.

The majority of the excess heat is added within 25 au where gas temperatures are over twice the original output from our thermochemical model. A likely source of this excess heat is mechanical heating from processes such as stellar winds or the dissipation of gravitational energy from accretion through the disk onto the star (e.g., Glassgold et al. 2004; Najita & Ádámkovics 2017). Mechanical heating from such phenomena is expected to be prominent in the inner disk (<10 au), and is not accounted for in RAC2D. Another possible heating source originates from polycyclic aromatic hydrocarbons (PAHs), as photoelectric heating of small grains (Draine & Li 2001; Li & Draine 2001) is one of the main heating mechanisms in this region after direct UV heating from the star. The PAH abundance might be enhanced in the inner disk if dust sintering is taken into account (Okuzumi et al. 2016). As dust grains pass the sublimation front of their constituent material, PAHs can be released, enhancing the effect of photoelectric heating near which ^{12}CO $2 - 1$ emits. PAH emission toward HD 163296 has been observed as a part of the Infrared Space Observatory Short Wavelength Spectrometer atlas (Sloan et al. 2003) and modeled by Seok & Li (2017). Their best-fit model uses a PAH abundance of $8 \times 10^{-7}\, M_{\oplus}$, which is 1.5× the abundance used in our RAC2D model. In our model and assumed physical setup, the excess heat is necessary in a region where the gas and dust are thermally coupled. Any increase in PAH abundance in our model will not change the temperature at which the majority of ^{12}CO $J = 2 - 1$ emits. It only affects the temperature in thermally decoupled layers where dust densities are low and gas and dust collisions do not occur often. However, it remains a possibility given an alternate setup of HD 163296 in which ^{12}CO $J = 2 - 1$ emits in the thermally decoupled layers.

3.3. Final Model

The model that best reproduces the CO radial profiles observed toward HD 163296 was achieved by altering the CO depletion profile derived by Z21, and increasing the gas temperature above a $z/r = 0.21$ within the inner 100 au of the disk. The CO radial profiles derived from the final model are shown in Figure 3 together with the observed profiles. The final gas and dust thermal structures are shown in Figure 4. Comparing the gas and dust temperatures, we find that below a $z/r \simeq 0.25$ the dust and gas are thermally coupled (with the exception of the increased gas temperature added artificially). Right above $z/r \simeq 0.25$ the dust is hotter than the gas by factors of 25%–50%. This region has been referred to as the "undershoot" region (Kamp & Dullemond 2004) and occurs in disks where the gas density increases sufficiently for line cooling to become very efficient, and occurs around the $\tau = 1$ surface. In our model, atomic oxygen dominates cooling in this region, and cooling via gas-grain collisions is particularly inefficient (see Figure 5). At the very surface of the disk, the gas temperature then increases drastically, overtaking the dust temperature significantly, which tends to plateau above the undershoot region. Directly above the undershoot region, photoelectric heating and the vibrational transitions of H_2 are the most significant heating processes, with direct heating of the gas via X-ray radiation overtaking them beyond $z/r \simeq 0.45$–0.5. This gas/dust temperature decoupling has been predicted (Kamp & Dullemond 2004; D'Alessio et al. 2005) and seen in models before (Tilling et al. 2012; Woitke et al. 2019; Rab et al. 2020).

It is worth noting that the C^{17}O and C^{18}O $1 - 0$ lines are the least well-fit to the observations. We also find that these transitions originate from deep within the disk, only slightly above the midplane, and CO snow surface. In Z21 it was noted that the C^{17}O column densities appear to be higher than those

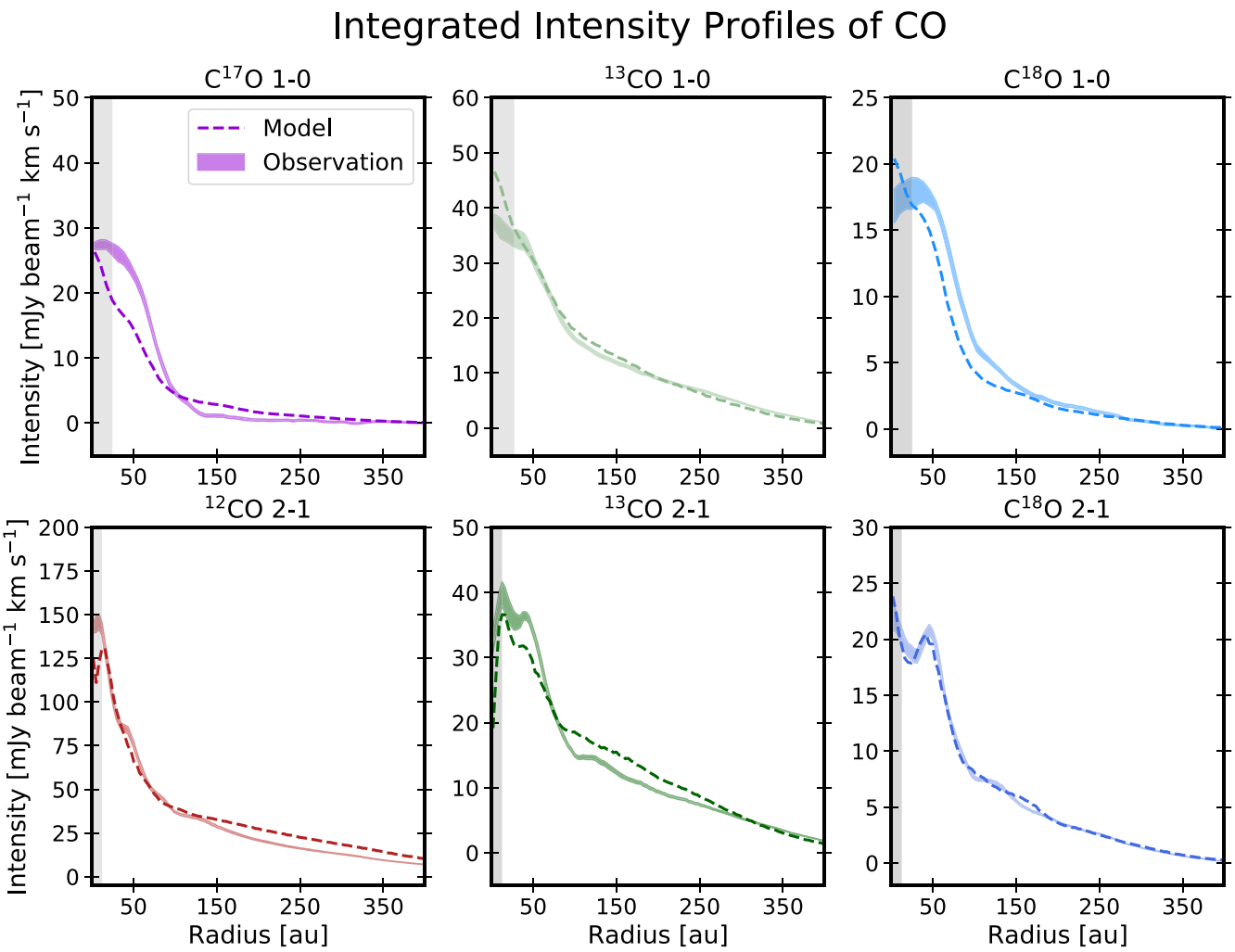

Figure 3. Integrated radial intensity profiles of ^{12}CO and its isotopologues ^{13}CO, C^{18}O, and C^{17}O as observed (solid line) and as simulated by the thermochemical code RAC2D (dashed line). The gray shaded regions correspond to the FWHM of the corresponding beam for each observed line. This presents our best-fit model to the observations of the HD 163296 disk and represents the thermal structure shown in Figure 4.

estimated from C^{18}O (correcting for optical depth). This is also the case for an earlier ^{13}C^{18}O detection, which appears to require a higher CO column than inferred from C^{18}O $J = 2 - 1$ (Z21). A similar analysis is preformed for the MAPS data in Z21. It is suggested that the CO abundance might be higher in the midplane as the icy pebbles drift inwards and sublimate CO inside the snowline. Booth et al. (2019) estimates a disk mass of 0.21 $M_{\odot}$ using ^{13}C^{17}O $J = 3 - 2$, a value 50% more massive than our final model. However, if CO is enhanced near the midplane, a larger mass may not be necessary. Such an effect is not accounted for in our analysis, but, at face value, would be consistent with our results in that a locally higher abundance of CO in the midplane, perhaps inside the CO snowline, would increase the emission of optically thin tracers (such as C^{17}O) while having a reduced effect on the emission of the more abundant isotopologues. This process has a negligible effect on the thermal structure as the dust and gas are strongly coupled in these layers.

3.3.1. CO and CO_2 Snowline

To determine the location of the CO snowline in our model, we determine the radial location at which there are equal parts CO frozen onto the dust and in the gas phase. RAC2D includes adsorption of CO (and other species) onto dust grains as well as desorption from the dust surface either thermally, or via UV photons or cosmic rays (see Du & Bergin 2014). Using this metric, our CO snowline is located at 60 au at a temperature of 18 K. This falls between the largest gaps in the continuum, and is consistent with Z21. Qi et al. (2015) used observations of N_2H^+ toward HD 163296 to determine the CO snowline as N_2H^+ formation is inhibited in the presence of gas-phase CO. When CO is frozen out N_2H^+ can exist, emitting as a ring with the innermost edge corresponding to the CO snowline. Using this method, and a model of the HD 163296 disk, they found a CO snowline at 74^{+7}_{-5} au (corrected for the pre-Gaia distance). Our midplane snowline location is in good agreement with the N_2H^+ derived snowline location, especially when considering findings from van't Hoff et al. (2017) that show the N_2H^+ column density peaks at 5 au or more beyond the midplane CO snowline. Additionally, we can predict the CO_2 snowline to be at 4 au, at a temperature of 65 K. These freeze-out temperatures depend on the given desorption energy. RAC2D uses values from Garrod et al. (2008), which assumed an amorphous ice surface. Assuming a different desorption energy will alter the derived snowline locations. It is important to also note that these snowlines are based on a thermochemical model

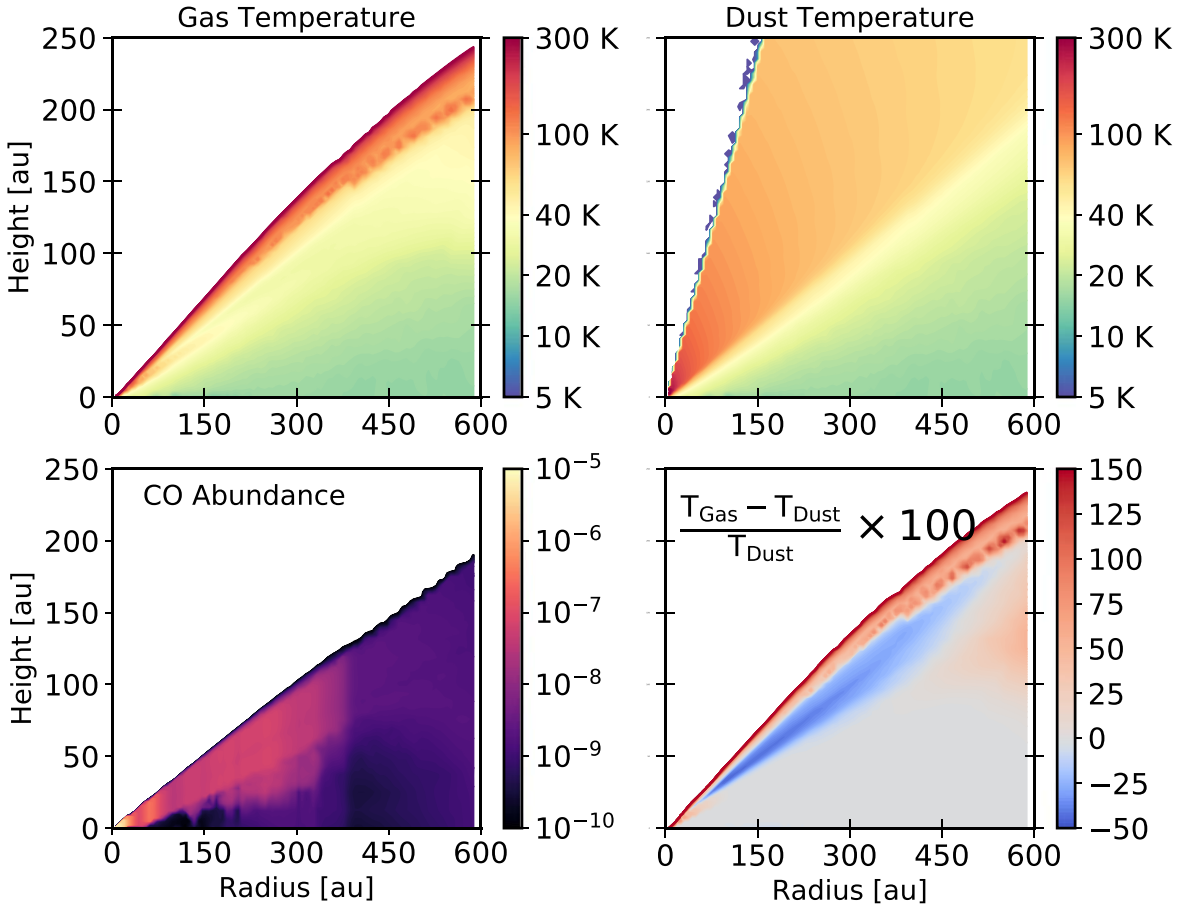

Figure 4. The two-dimensional profile of gas temperature, dust temperature, percentage difference between the two, and CO abundance. The dashed black or white lines in each plot show where $z/r = 0.21$, which corresponds with the ^{12}CO $J = 2 - 1$ surface within 100 au. This represents the model that best represents the observed radial profile, SED, and an HD flux that agrees with the currently derived upper limit. In the percentage difference plot, one can see where the dust and gas temperatures are coupled (gray), the "undershoot" region (Kamp & Dullemond 2004), where dust is warmer than the gas (blue), and where gas is warmer high up in the atmosphere (red).

influenced by observations that do not directly probe the midplane.

4. Discussion and Analysis

4.1. Emitting Surface

An additional observational constraint on our model is the resolved emission heights of ^{12}CO, ^{13}CO, and C^{18}O $J = 2 - 1$ as measured in Law et al. (2021b). We calculate the emitting surfaces of ^{12}CO, ^{13}CO, and C^{18}O using simulated image cubes and the same methods as applied to the observations by Law et al. (2021b). This method depends on the ability to resolve the front and back side of a given disk over multiple channels of an image cube, and assumes azimuthal symmetry and gas rotating in circular orbits (Pinte et al. 2018). The emitting height extraction tools are found in the Python package DISKPROJECTION.[28] A comparison of the emitting layers of our model and observations is shown in Figure 6.

The calculated emitting layers for both simulated and observed data from Law et al. (2021b) exist at similar heights, and agree within 1σ at most radii. No additional changes to the model were necessary to arrive at this agreement between the model and observation. Our modeled emission height for ^{12}CO $J = 2 - 1$ reproduces what was derived using the ALMA observations up until ∼125 au; beyond this radius and up to 250 au, the model's ^{12}CO emits on average 11 au lower in the disk. When looking at the ^{13}CO-emitting height, the model reproduces the observed heights beyond ∼125 au. This suggests that our model does not completely represent the CO vertical distribution, as it systematically produces a lower ^{12}CO $J = 2 - 1$ emission height beyond ∼100au. However, this fit is quite good considering the detailed physics and chemistry included in the model. The C^{18}O emitting heights agree well with what is observed, especially within ∼100 au, where both our model and the observations pick up on some substructure, a bump at 70 au, and subsequent dip at 85 au. Our model shows another increase in the C^{18}O emission height at 110 au, not present in the ALMA observations, a feature created due to relative CO abundance based on our depletion profile (see Figure 1).

4.2. Comparison to Empirical Temperature Structure

In Law et al. (2021b), radial brightness temperatures (T_B) are calculated for each of the CO $J = 2 - 1$ isotopologue lines, with a resolution of a quarter of the beam size. Here, we derive the brightness temperature of our model using an identical procedure to enable a consistent comparison. We compare the empirically derived temperatures for each of the $J = 2 - 1$ lines in Figure 7. At most radii, the model's derived brightness temperature agrees within 10% of the observed brightness

[28] https://github.com/richteague/diskprojection

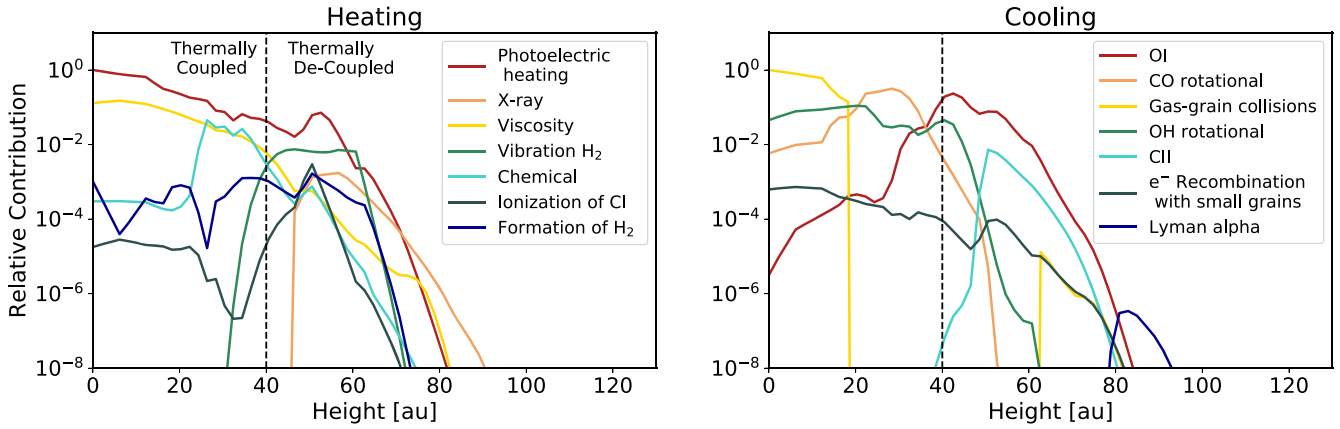

Figure 5. The seven most significant heating (right) and cooling (left) mechanisms in our final model at a disk radius of 150 au, as a function of disk height, normalized according to the highest heating/cooling value at this radius. The black dashed line corresponds to the height (40 au) at which the dust and gas temperatures become decoupled.

temperature. Regions where the brightness model temperature is less than ∼20% of the observed T_B corresponds to regions where the emitting heights diverge. For example, in the ^{12}CO comparison, the brightness temperature derived from the model is 20% less than the observed value starting at ∼125 au, precisely where the ^{12}CO-emitting heights diverge and the model ^{12}CO-emitting height is 11 au deeper in the disk, where temperatures are cooler. Brightness temperatures measured from ^{13}CO are in good agreement, up until ∼250 au. Beyond ∼250 au the model's emitting height sharply decreases while the observed emitting heights stay relatively constant (although with a large uncertainty), which explains the large disconnect between the model and observed brightness temperatures. The average brightness temperature derived from ALMA observations of C^{18}O is 24 K, thus at radii where the model differs from the observed brightness temperature the most (∼20% less than observed), it is by just 4–5 K. Based on these comparisons, we show that this temperature structure based on a model derived by matching radial intensity profiles of CO, the disk SED, and unresolved fluxes of HD and upper transitions of CO, reproduces the observed brightness temperatures relatively well.

4.3. Implications for Disk Mass

This model uses a disk mass of 0.14 $M_\odot$. However, there is a degeneracy between the CO and H_2 surface densities. Increasing one parameter while decreasing the other by the same factor produces a model that reproduces radial profiles in CO nearly identical to the original model (Calahan et al. 2021). Any change in heating based on the H_2 or CO mass (heating via H_2 formation, H_2 and CO self-shielding) will not significantly affect the regions where the dust and gas temperatures are coupled. This applies to the vast majority of the disk, and where the bulk of the HD flux originates. Observing the flux of the HD molecule is a way to break this degeneracy and directly probe mass, as its ratio to H_2 is well understood (Linsky 1998). Unfortunately, there was a non-detection of HD toward HD 163296 when observed with the PACS instrument on Herschel (Pilbratt et al. 2010; Poglitsch et al. 2010). Kama et al. (2020) provides 3σ line flux upper limits for the HD $1-0$ and $2-1$ lines, 6.0×10^{-18} W m^{-2} and 3.0×10^{-18} W m^{-2}, respectively. Our model predicts an HD $1-0$ flux of 3.3×10^{-18} W m^{-2} and a $2-1$ flux of

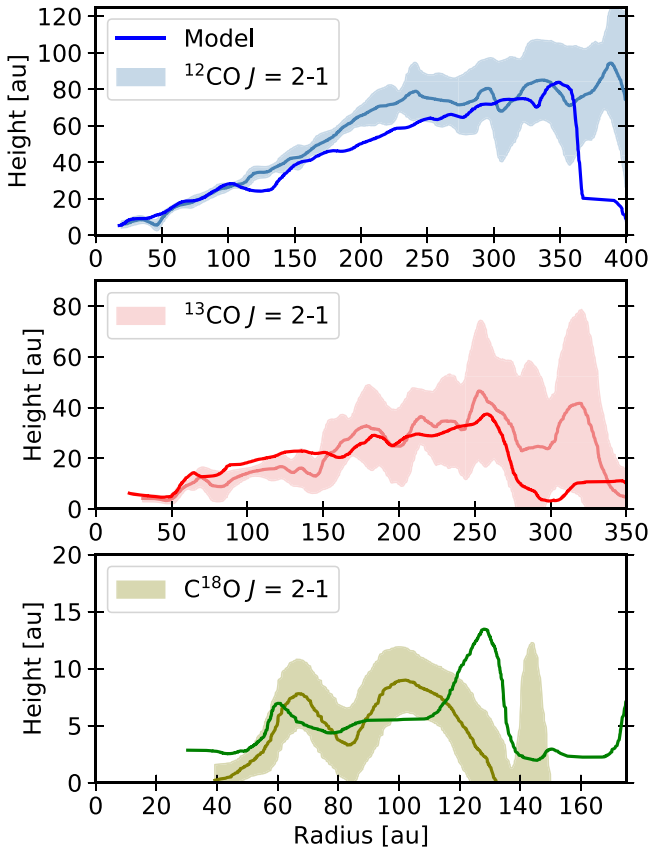

Figure 6. Derived emitting surfaces and calculated uncertainties of the $2-1$ transitions of ^{12}CO, ^{13}CO , and C^{18}O. Observed emitting surfaces with calculated errors are shown in blue, red, and green from Law et al. (2021b) while the model emitting surfaces are shown by the brighter blue, red, and green lines without accompanying errors.

8.26×10^{-19} W m^{-2}. While it remains below the flux upper limit, this results in considerable uncertainty in the mass.

To determine an upper mass limit, we use our final model and increase the disk gas mass while decreasing the CO abundance by the same factor. Due to the degeneracy between H_2 and CO, we can continue to reproduce the observed CO radial profiles while increasing the mass of the disk. An HD 163296 disk model with a mass of 0.35 $M_\odot$ produces a predicted HD $1-0$ flux of 5.9×10^{-18} W m^{-2} and a $2-1$

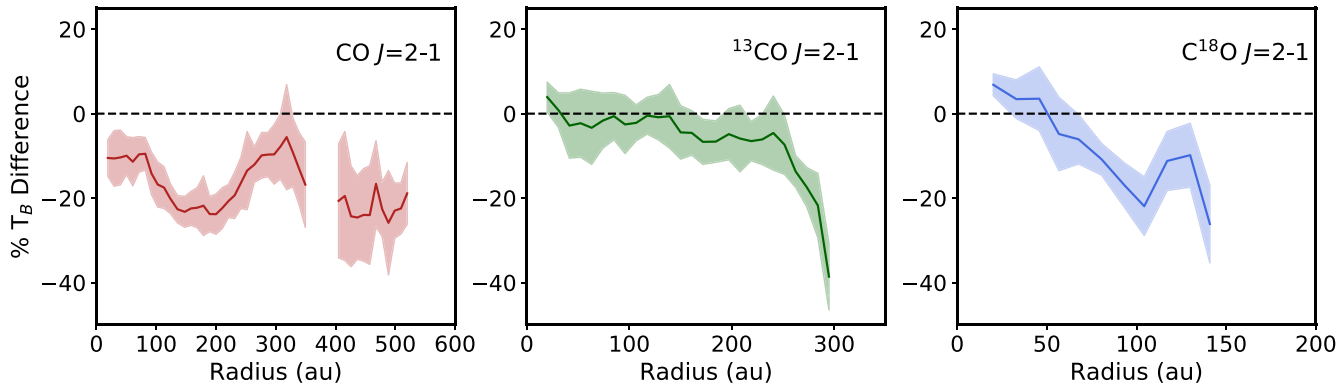

Figure 7. A comparison of the derived brightness temperature from the HD 163296 disk model and ALMA observations (Law et al. 2021b). The *y*-axis shows the percentage difference between derived brightness temperature from the model and the ALMA results ($\frac{T_{\rm rac2d} - T_{\rm obs}}{T_{\rm obs}} \times 100$). The error is plotted as the shaded region and is motivated by the 1σ uncertainty in the observed brightness temperature ($\frac{T_{\rm rac2d} - T_{\rm obs} \pm \Delta T_{\rm obs}}{T_{\rm obs}} \times 100$).

flux of 2.0×10^{-18} W m^{-2}. This is our upper mass limit, as constrained by the HD flux. This upper mass limit is higher than the majority of mass estimates for HD 163296, and lower than the largest estimate for HD 163296 which is 0.58 $M_\odot$ from Woitke et al. (2019). A more recent estimation for HD 163296 is presented in Booth et al. (2019) using the optically thin CO isotopologue, ^{13}C^{17}O, and predicts a mass of 0.21 $M_\odot$. This is a higher mass than we use in our model, but is also consistent with the HD flux limits and our thermochemical model. Using their derived HD flux limits, Kama et al. (2020) determined an mass limit for the disk of $\leqslant$0.067 $M_\odot$. They created a disk model that reproduced dust observations and a number of unresolved rotational transitions of ^{12}CO as well as a resolved observation of ^{12}CO $J = 3 - 2$. There are two significant differences between our physical models that could explain the disparity between our calculated upper mass limits. Their HD 163296 model uses a star with a luminosity of 31 $L_\odot$ (Folsom et al. 2012) while this model uses a much lower luminosity of 17 $L_\odot$ (Fairlamb et al. 2015). Additionally, they do not deplete CO which acts as a gas coolant, namely in the decoupled thermal regions, leading to a slightly cooler disk than ours. The contrast between our two models using the same HD flux observation to derive different disk-mass estimates highlights the importance of a well-defined temperature structure.

4.4. Implications for Gap Thermochemistry

The temperature of gas in potentially planet-carved gaps can provide an insight into planet formation models directly linking protoplanetary disk environments to planet formation theories. The effects of disk geometry on temperature have been studied previously and it has been shown that the properties of local perturbations in the disk, including gap size and depth, radial location from the star, and disk inclination, will have an effect on the temperature structure (Jang-Condell 2008). Gaps have been found to be either cooler or warmer than the surrounding medium, dependent on disk geometry and other model assumptions. A decrease in the gas and small dust surface densities exposes material in and near the midplane to more UV flux, allowing for an increase in the temperature of both the gas and dust (van der Marel et al. 2018; Alarcón et al. 2020), however puffed-up walls can produce shadows cooling the disk midplane (Nealon et al. 2019) or the gas-to-dust ratio can be low enough to decouple gas and dust temperatures heating only the dust (Facchini et al. 2018). Using our final model, we explored the effect that corresponding gaps in the gas and small dust in HD 163296 may have on the presumed CO depletion, and subsequent gap-temperature effects.

The gaps observed in the continuum emission in the HD 163296 disk are accounted for in the surface density of the large grains in our model. Meanwhile, the gas and small dust surface densities are smooth, and do not account for these gaps. This is a deliberate decision, as a primary goal of this study is to constrain the global thermal properties of the gas disk in general. We find that even with a smooth H_2 gas distribution, the location of the gaps in the large-dust population are warmer than outside of the gap by an order of a few kelvin. This is supported by previous studies of the HD 163296 disk (van der Marel et al. 2018; Rab et al. 2020) which also find an increased temperature at gap locations using thermochemical models and observations of the gas and dust.

Gaps are often attributed to ongoing planet formation. To determine the gas and small-dust depletion level within the gap, we created four models representing two of the gaps and two possible planet masses. The most prevalent gaps in the continuum (the widest and highest contrast gaps) are located at 48 au and 86 au. The location, depth, and width of the gas and small-dust gap used in our model is motivated by the measured gap widths in continuum from Isella et al. (2018) and the predicted planet masses from Zhang et al. (2018) that are dependent on dust size distribution and viscosity. We set gap depths, parameterized by a depletion of H_2 gas within the gap, using two assumed planet masses, 1 $M_{\rm J}$, which represents a typical planet mass estimate for the HD 163296 disk (Pinte et al. 2018; Teague et al. 2021), and 4.45 $M_{\rm J}$, which represents the highest-mass planet predicted within HD 163296 (Zhang et al. 2018). We used Equation (5) in Kanagawa et al. (2015) to determine gap depth using our model's density distribution, viscosity ($\alpha = 10^{-2}$), and planet mass. A 1 $M_{\rm J}$ planet at 48 au leads to a gas depletion depth of 23%, and at 86 au, 19%. A 4.45 $M_{\rm J}$ planet at 48 au leads to a gas depletion depth of 85%, and at 86 au, 82%.

We use our final HD 163296 disk model and rerun it with the new gas surface density dependent on gap location and planet mass. The two models with a gap from a 1 $M_{\rm J}$ planet produce a negligible change in the observed radial intensity profile, while a model with gap depths corresponding to a 4.45 $M_{\rm J}$ planet shows a significant decrease in flux, see Figure 8. We then calculate a new CO depletion profile in order for the models with a 4.45 $M_{\rm J}$ planet-induced gap to match the observed radial

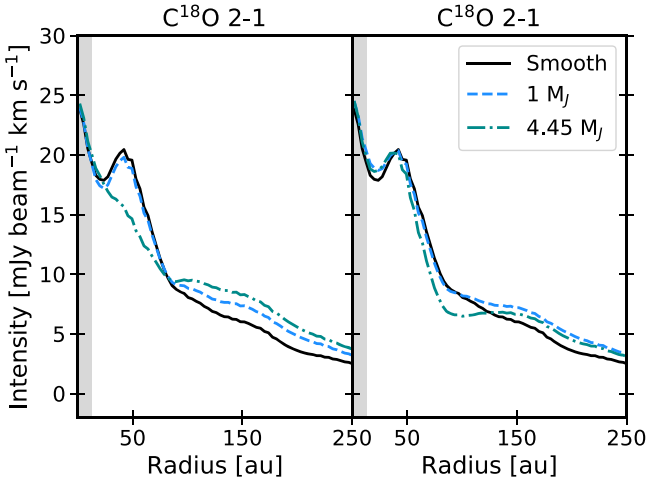

Figure 8. $C^{18}O$ $J = 2 - 1$ radial profiles for a smooth model (black), a model with a gap in the small-dust and gas population that corresponds to a 1 M_J planet (blue dashed), and a 4.45 M_J planet (teal dashed). The left panel shows the results for a gap centered at 48 au, and the right panel is for a gap at 86 au.

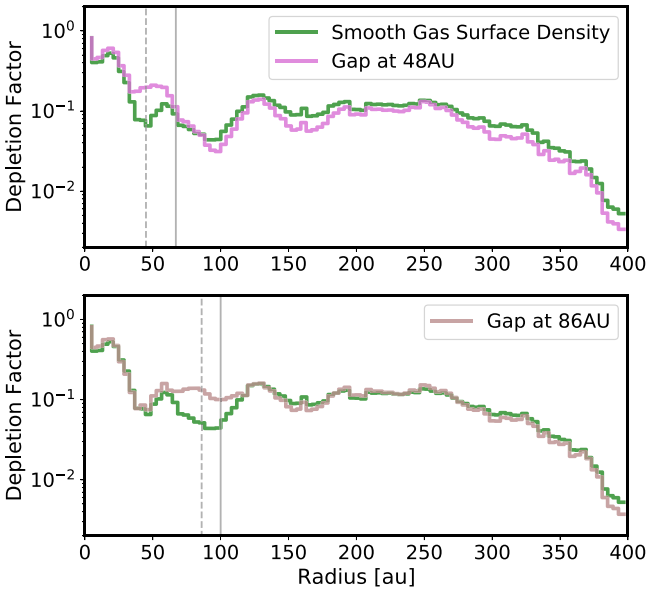

Figure 9. The calculated CO depletion for a smooth surface density model (green), and for a model with a gap at 48 au (top, pink) and 86 au (bottom, dark pink). The dashed gray lines correspond to the center of a gap, and the solid gray line corresponds to a ring. When imposing a gap in the total surface density, the CO depletion is flat or enhanced as opposed to being a local minimum at the location of the gap.

emission profile. Those profiles are show in Figure 9. Previously, with a smooth gas distribution, the CO depletion profile had local minima at the location of the gaps. In the case of gas and small dust surface densities with deep gaps, the CO abundance increases at the location of the gaps, bringing it to a level on par with the depletion factors just outside of the gaps. Our method of CO depletion makes it difficult to disentangle chemical/gap effects on the CO abundance, so it is impossible to discern if this relative increase in CO in the gaps is an enhancement or a leveling off to a more constant CO depletion across the radius. Studies such as Alarcón et al. (2020) and van der Marel et al. (2016) have predicted that CO enhancement in the gaps is needed to match observations. One possible mechanism to enhance the CO abundance is the presence of

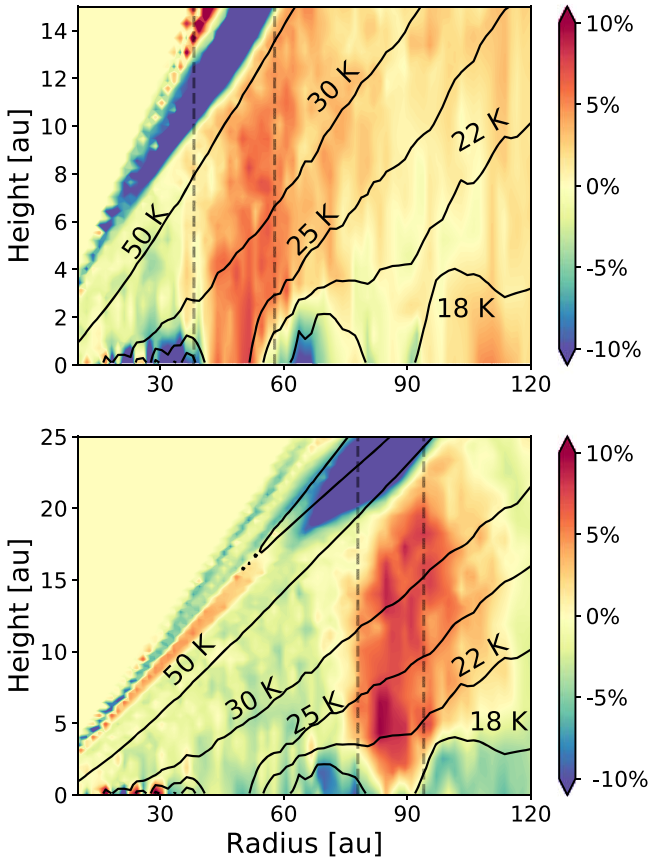

Figure 10. A comparison of gas temperatures between a model with a smooth gas surface density, and a model that has a gap in the gas at 48 au or 86 au. Both models have gaps in the large-dust population and both models match observed radial profiles of CO, following CO depletion profiles seen in Figure 9. Contour lines show gas temperatures of the smooth gas surface density model. The background corresponds to percentage difference from the smooth surface density model. Positive values imply a hotter temperature in the gas-gap models, negative values indicate a hotter temperature in the smooth model. The dashed black lines correspond to the gap width.

meridional flows found at the gaps in HD 163296 by Teague et al. (2019), which can transport gas and small grains from the upper atmosphere, bringing CO sublimating from grains and a rich chemistry to an otherwise chemically inert midplane. Whether or not CO is enhanced locally, is dependent on the depth of the gas gap. At present, the best method to determine gas depletion in gaps is to use kinematics to constrain the H_2 pressure gradients (Teague & Foreman-Mackey 2018) and thus the amount of CO chemical processing that might be happening (Alarcón et al. 2021)

Using the new CO depletion profiles for our deep gas-gap models, we find that the gap temperature increases by upwards of 10% compared to a model with a smooth gas surface density. Figure 10 shows the difference in temperature between our smooth gas model and our gapped models, both of which match the observed CO radial profiles. The increase in temperature in the gap arises due to the decreased UV opacity from the depletion of small grains, allowing more flux to enter the region. There is a region in the atmosphere above the heated layer that is cooler than a smooth gas surface density model by over 10%. This occurs at the undershoot region where the gas temperature is lower than the dust temperature due to atomic lines becoming major coolants. In the gas-gap models, this cooler, optically thick layer is at a slightly lower height.

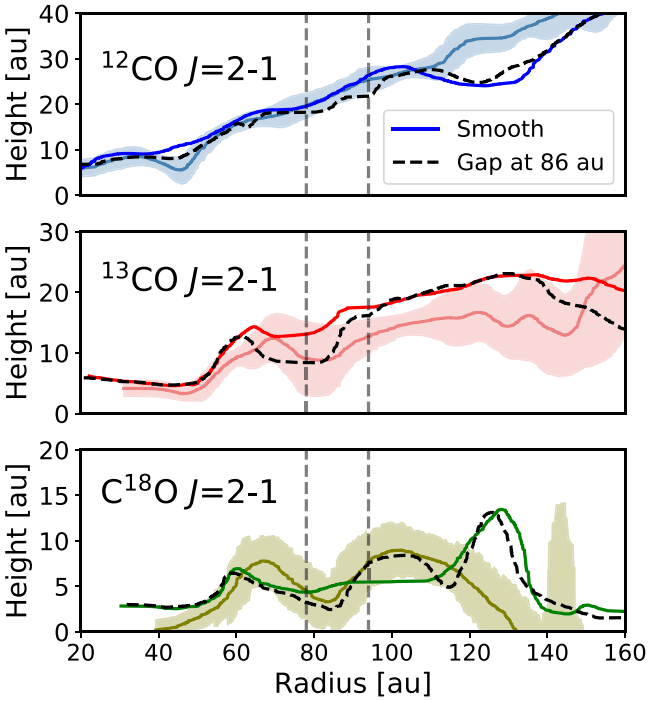

Figure 11. Emitting surface of ^{12}CO, ^{13}CO, and C^{18}O $J = 2 - 1$ in a model that uses a depletion of CO (solid line), and a model that has a gap in the gas surface density at 86 au (dashed black line) as compared to observations (thick line).

We also compare the observed emitting surface of the CO $J = 2 - 1$ line to the model with a deep gap at 86 au in Figure 11. There is limited emitting-surface information for C^{18}O $J = 2 - 1$ at the location of the 48 au gap, thus we focus on the gap farthest out. The models with 1 M_J planet gaps showed very little variation compared to the smooth model. The 4.45 M_J model provides the best insight into how a significant deviation in the gas surface density could affect the emitting surface and the degeneracy between the H_2 surface density and CO abundance. At the location of the gap, each CO isotopologue $2 - 1$ transition emits from a lower layer, with ^{13}CO and C^{18}O showing the strongest change in height (<6 au). This suggests that in highly gas-depleted gaps the degeneracy between the H_2 surface density and CO abundance can be broken. An even more significant difference between the two models is highlighted in the C^{18}O $J = 2 - 1$ emitting surface. Just beyond the gap at 86 au, the model with a deep gap in the surface density follows the observed emitting surface more so than the model with a smooth surface density and structured CO depletion profile. Exploring the limits of the degeneracy between CO and H_2 is beyond the scope of this study, however extracting and comparing observed and simulated emitting surfaces may be an interesting tool to use in the future.

5. Conclusions

Using high spatial resolution observations of ^{12}CO $J = 2 - 1$, ^{13}CO $J = 2 - 1$, $1 - 0$, C^{18}O $J = 2 - 1$, $1 - 0$, and C^{17}O $1 - 0$ from the ALMA-MAPS large program in concert with the thermochemical code RAC2D, we derive a 2D thermal structure for the disk around the Herbig Ae star HD 163296. Our conclusions are the following:

1. We derived a 2D thermal structure for the disk around the Herbig Ae star HD 163296 that reproduces six spatially resolved rotational transition lines of CO and its isotopologues, in addition to the observed SED and structures observed in the continuum, the predicted HD flux remains below the observed upper limit, and we reproduce observed fluxes of 19 higher J-level transitions of ^{12}CO.
2. The derived temperature agrees well with empirically derived temperatures and calculated emitting heights. This temperature structure represents the full 2D thermal structure, filling in temperature information at spatial locations, which observations do not directly probe.
3. We calculate a CO depletion profile which shows a relative enhancement of CO within the CO snowline, a slightly lower depletion value between the CO snowline and 250 au, and then a significant drop off that can be explained via CO chemical processing.
4. Using the derived thermal structure, we predict a midplane snowline location for CO of 60 au which corresponds to a freeze-out temperature of 18 K. We also find an upper mass limit of 0.35 $M_\odot$.
5. The temperature is locally enhanced in the millimeter continuum gaps at 48 and 86 au. This is true both for gaps consisting of only large-grain depletion, and those with large-grain, small-grain and gas depletion. The temperature within the gap increases slightly when gas and small dust are depleted in addition to large grains, by at most 10% in the case of significant depletion.

This paper makes use of the following ALMA data: ADS/JAO.ALMA#2018.1.01055.L. ALMA is a partnership of ESO (representing its member states), NSF (USA) and NINS (Japan), together with NRC (Canada), MOST and ASIAA (Taiwan), and KASI (Republic of Korea), in cooperation with the Republic of Chile. The Joint ALMA Observatory is operated by ESO, AUI/NRAO and NAOJ. The National Radio Astronomy Observatory is a facility of the National Science Foundation operated under cooperative agreement by Associated Universities, Inc.

J.K.C. acknowledges support from the National Science Foundation Graduate Research Fellowship under grant No. DGE 1256260 and the National Aeronautics and Space Administration FINESST grant, under grant No. 80NSSC19K1534. E.A.B. acknowledges support from NSF AAG grant #1907653. K.Z. acknowledges the support of the Office of the Vice Chancellor for Research and Graduate Education at the University of Wisconsin–Madison with funding from the Wisconsin Alumni Research Foundation, and the support of NASA through Hubble Fellowship grant HST-HF2-51401.001 awarded by the Space Telescope Science Institute, which is operated by the Association of Universities for Research in Astronomy, Inc., for NASA, under contract NAS5-26555. K.R.S. acknowledges the support of NASA through Hubble Fellowship Program grant HST-HF2-51419.001, awarded by the Space Telescope Science Institute,which is operated by the Association of Universities for Research in Astronomy, Inc., for NASA, under contract NAS5-26555. K.I.Ö. acknowledges support from the Simons Foundation (SCOL #321183) and an NSF AAG grant (#1907653). R.T. and F.L. acknowledge support from the Smithsonian Institution as a Submillimeter Array (SMA) Fellow. J.D.I. acknowledges support from the Science and Technology Facilities Council of the United Kingdom (STFC) under ST/T000287/1. C.J.L. acknowledges funding from the National Science Foundation Graduate Research Fellowship under grant DGE1745303. R.L.G. acknowledges support from a CNES fellowship grant. M.L.R.H. acknowledges support from the Michigan Society of Fellows. Y.A. acknowledges support by NAOJ ALMA Scientific Research grant code 2019-13B

and Grant-in-Aid for Scientific Research (S) 18H05222. S.M.A. and J.H. acknowledge funding support from the National Aeronautics and Space Administration under grant No. 17-XRP17 2-0012 issued through the Exoplanets Research Program. Support for this work was provided by NASA through the NASA Hubble Fellowship grant #HST-HF2-51460.001-A awarded by the Space Telescope Science Institute, which is operated by the Association of Universities for Research in Astronomy, Inc., for NASA, under contract NAS5-26555. J.B. acknowledges support by NASA through the NASA Hubble Fellowship grant #HST-HF2-51427.001-A awarded by the Space Telescope Science Institute, which is operated by the Association of Universities for Research in Astronomy, Incorporated, under NASA contract NAS5-26555. C.W. acknowledges financial support from the University of Leeds, STFC, and UKRI (grant Nos. ST/R000549/1, ST/T000287/1, MR/T040726/1). I.C. was supported by NASA through the NASA Hubble Fellowship grant HST-HF2-51405.001-A awarded by the Space Telescope Science Institute, which is operated by the Association of Universities for Research in Astronomy, Inc., for NASA, under contract NAS5-26555. F.M. acknowledges support from ANR of France under contract ANR-16-CE31−0013 (Planet-Forming-Disks) and ANR-15-IDEX-02 (through CDP "Origins of Life"). G.C. is supported by the NAOJ ALMA Scientific Research grant code 2019-13B. V. V.G. acknowledges support from FONDECYT Iniciación 11180904 and ANID project Basal AFB-170002. F.A. acknowledges support from NSF AAG grant No. 1907653. J.B.B. acknowledges support from NASA through the NASA Hubble Fellowship grant No. HST-HF2-51429.001-A, awarded by the Space Telescope Science Institute, which is operated by the Association of Universities for Research in Astronomy, Inc., for NASA, under contract NAS5-26555. A.S.B acknowledges the studentship funded by the Science and Technology Facilities Council of the United Kingdom (STFC). A.D.B. acknowledges support from NSF AAG grant No. 1907653. H.N. acknowledges support by NAOJ ALMA Scientific Research grant code 2018-10B and Grant-in-Aid for Scientific Research 18H05441. Y.Y. is supported by IGPEES, WINGS Program, the University of Tokyo.

We also thank the referee for a careful read of the text and insightful comments.

Facility: ALMA

Software: RAC2D (Du & Bergin 2014), bettermoments (Teague & Foreman-Mackey 2018), GoFish (Teague et al. 2019), diskprojection (https://github.com/richteague/diskprojection), CASA (McMullin et al. 2007), RADMC3D (Dullemond et al. 2012), scipy (Virtanen et al. 2020), Matplotlib (Hunter 2007), Astropy (Astropy Collaboration et al. 2013, 2018)

Appendix A
Parameter Exploration Analysis

Our model of the HD 163296 disk based on the density structure from Z21 with an updated CO depletion profile reproduces radial profiles from all lines except ^{12}CO $J = 2 - 1$ relatively well (see Figure A1). Thus, this initial model appears

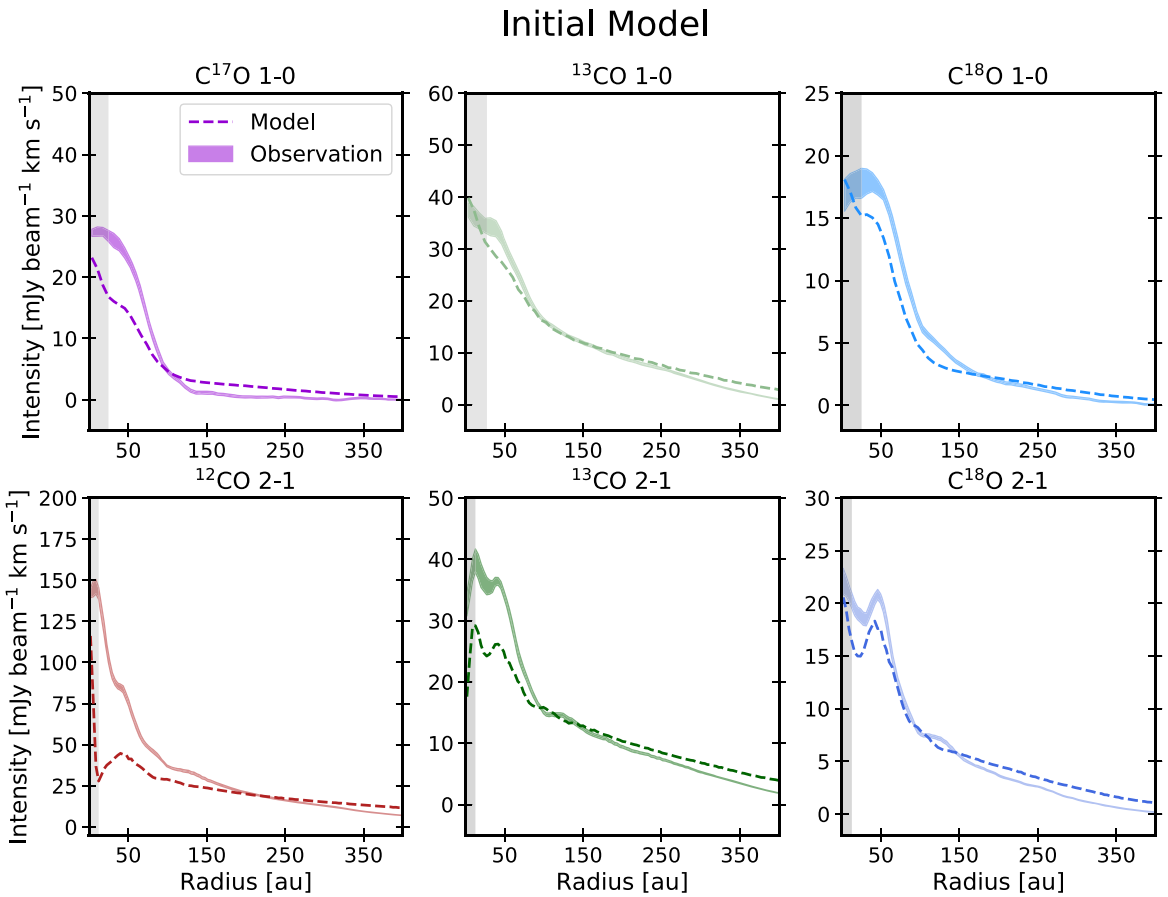

Figure A1. Radial emission profiles as predicted by the initial HD 163296 model based on Z21 compared to the observed profiles (solid line). Parameters are listed in Table 3. This model uses the CO depletion calculated in Z21, applied before the temperature calculation. The chemistry runs for 0.01 Myr and this model lacks the excess heating found necessary to reproduce the ^{12}CO $J = 2 - 1$ observation.

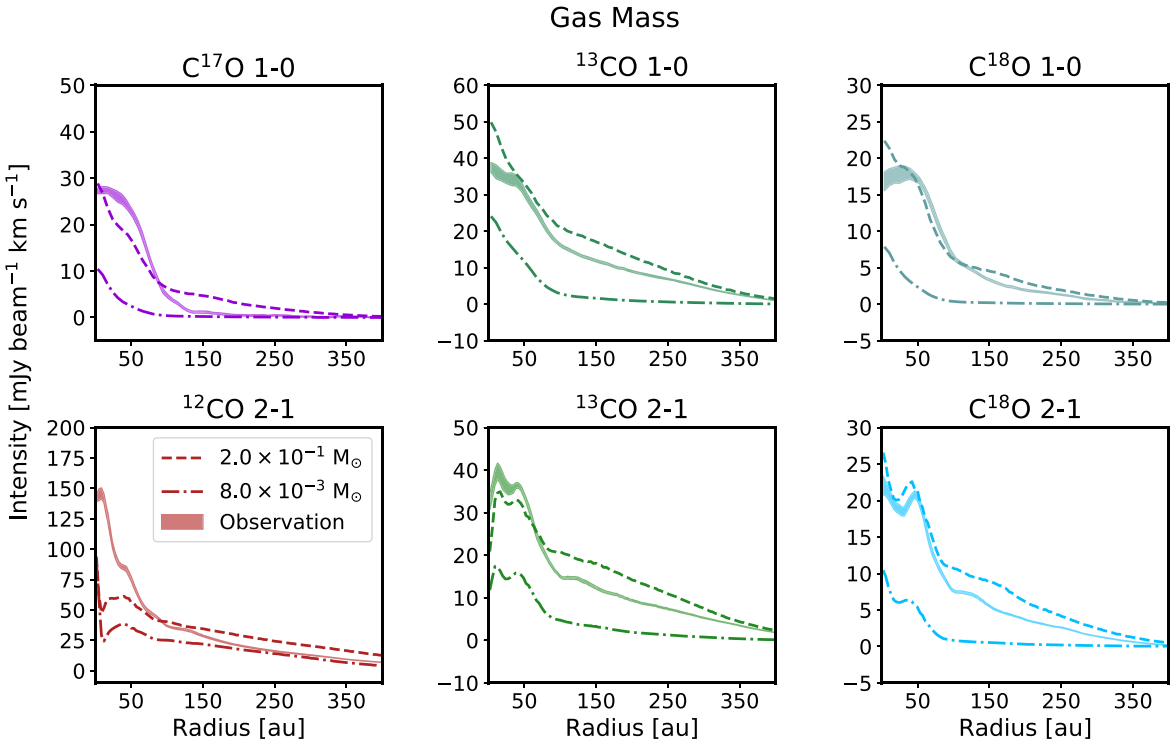

Figure A2. Modeled radial emission profiles of the HD 163296 model based on Z21 compared to the observed profiles (solid line). These models exhibit a varying gas mass of 0.2 $M_{\odot}$, which is a mass prediction for HD 163296 by Booth et al. (2019), and 0.008 $M_{\odot}$, which is the smallest predicted mass in the literature. The radial profiles of models with the highest and lowest values in our parameter exploration are compared to observations.

(The complete figure set (7 images) is available.)

to roughly represent the 2D thermal structure, but cannot reproduce the disk layers at which ^{12}CO $J = 2 - 1$ emission originates, as this line is underpredicted by a factor of about 2 within the brightest region (within 50 au). However, improvements can be made to all lines except for C^{18}O $J = 2 - 1$ (and arguably ^{13}CO $1 - 0$) because they are slightly underpredicted in the inner 75 au, while slightly overpredicted in the outer disk. In order to achieve a more complete and accurate thermal profile, it is worth exploring the sensitivity of the radial emission profiles to the disk physical parameters.

Throughout the parameter exploration, we did not alter the CO depletion profile. We find that the CO depletion is only degenerate with disk physical parameters that affect the total gas mass or mass distribution (γ). When the scale height, characteristic radius, or flaring parameter are changed, we find that there is no single CO depletion profile that brings all lines of CO toward what is observed.

We ran a set of models that explored the parameter space of gas mass, small-dust mass, flaring parameter (Ψ), surface density power index (γ), characteristic radius (r_c), critical height (h_c), and radial extent and allowed for the temperature to evolve in a new physical environment. Because HD 163296 has been widely studied, we determined the range exploration based on literature values. There has been a wide array of gas-mass estimates, from as low as 8×10^{-3} up to 0.58 $M_{\odot}$ (Isella et al. 2007; Williams & Best 2014; Boneberg et al. 2016; Miotello et al. 2016; Williams & McPartland 2016; Booth et al. 2019; Powell et al. 2019; Woitke et al. 2019; Kama et al. 2020). Our initial gas mass is 0.14 $M_{\odot}$, which is on the higher end, thus we created three models that are lower in mass, and one higher in mass: 8×10^{-3}, 1×10^{-2}, 6.7×10^{-2} (predicted gas upper limit based on the HD $1 - 0$ flux (Kama et al. 2020)), and 0.21 $M_{\odot}$ (the HD 163296 disk-mass estimate from Booth et al. 2019). In terms of small-dust mass, the SED constrains the range of exploration. We start with a mass of 1×10^{-4} $M_{\odot}$, and explore values above and below this with the extremes being clear under- and overpredictions of the SED flux beyond 10 μm: 1×10^{-6} $M_{\odot}$, 1×10^{-5} $M_{\odot}$, 1×10^{-3} $M_{\odot}$, and 1×10^{-2} $M_{\odot}$. Flaring for HD 163296 has also had a wide range of estimates throughout the literature, and different studies assume both flat and flared disks. We explore models that use Ψ values above and below what we have used (1.08). This includes 0.05, 1.0, 1.6, and 2.2 (Tilling et al. 2012; de Gregorio-Monsalvo et al. 2013; Woitke et al. 2019; Kama et al. 2020).The surface density index, γ, has a natural limit in our description of surface density (see Equation (1)). We explore values above and below our initial value of 0.8: 0.2, 0.6, 1.2, and 1.8. There is ^{12}CO $J = 2 - 1$ detected out to 600 au, thus we only explored values above that for r_{out}: 700, 1000, and 1200 au. For r_c and h_c we explore four values, the lowest of which corresponds to the millimeter-dust distribution, and the largest being double our initially inferred value.

Changes in gas mass, small-dust mass, and scale height have similar effects on the CO radial profiles, increasing or decreasing the CO intensity with increasing/decreasing gas mass and scale height and decreasing/increasing small-dust mass. Changing the scale height will increase or decrease the CO flux along all radii for all transitions (see Figure A2), while small-dust mass and gas mass affect some lines more than others (see Figure A2). For example, changes in the mass of the gas or small-dust populations do not have as strong an effect on ^{12}CO J 2 $-$ 1 as they do on nearly every other line. While mass changes in these two populations appear to have similar effects, any degeneracy between the two can be broken as the small-dust population is constrained by the SED.

As the flaring parameter, Ψ, increases, emission is enhanced in the outer disk (the divide between "outer" and "inner" disk depends on the characteristic radius). As Ψ decreases, there is a significant increase in the inner disk (see Figure A2). We found for this model that even small changes in Ψ strongly affect the final radial profile across all lines. The surface density power index, γ, tends to leave the flux in the inner few astronomical units unaffected, but with a smaller γ more emission can be found farther out in the disk (see Figure A2). This is due to the fact that a smaller γ produces a population that is more evenly distributed. The characteristic radius affects both the height and surface density of a given population, with lower r_c values producing a rapid increase in height and a turn over the surface density at a shorter radius (see Figure A2). The combination of these two effects produces radial profiles that are brighter for smaller critical radii. The outer radius values we explored did not produce significantly different CO radial profiles, due to the fact that the majority of the emission from all lines exists within 400 au, thus an outer radius cutoff well beyond this limit does not affect the observed emission (see Figure A2).

After this exploration of parameter space, and subsequently creating a number of models that altered multiple parameters simultaneously, we determined that the best set of parameters were the ones that were used by Z21. Keeping with these values, the derived thermal structure matches five out of six of the radial intensity profiles relatively well and is the best χ^2 fit for the SED (as per Z21).

Appendix B
Gas-temperature Structures in HD 163296 Models from the Literature

There has been one other recent attempt to characterize the 2D thermal structure of the HD 163296 disk specifically, using a thermochemical code, matching multiple line observations and the SED. Those results are presented in Woitke et al. (2019). They use the thermochemical code ProDiMo (PROtoplanetary DIsk MOdel; Woitke et al. 2009; Kamp et al. 2010; Woitke et al. 2016) and derive a disk model that reproduces observed line fluxes from infrared to millimeter wavelengths within a factor of about 2, along with the observed SED. The model outputs from Woitke et al. (2019) are available publicly, and we compare our final thermal structure to their results in Figure B1. The dust temperatures in both models are very similar, with the disk in our model being slightly more flared. The gas temperatures are very similar within ~200 au, while past 300 au the ProDiMo model has a much hotter disk than what this study predicts. That relatively hot temperature most likely would affect the spatially resolved radial profiles, namely ^{12}CO $J = 2 - 1$ which emits beyond 300 au.

There are a few possible reasons as to why that study did not find it necessary to invoke additional heating in the layers at which ^{12}CO $J = 2 - 1$ primarily emits. A key difference between the two models is the underlying gas mass: 0.58 $M_\odot$ from Woitke et al. (2019) versus 0.14 $M_\odot$ in this study (although the ProDiMo model used a pre-Gaia distance of 119 pc, as opposed to the Gaia-determined 101 pc). Additionally, the ProDiMo model utilizes an enhanced gas/dust ratio of >100 throughout the whole disk, and an even higher ratio within the inner few astronomical units. In our case, depleting small dust within the inner disk (tens of astronomical units) in our model did not appear to rectify the difference between predicted and observed ^{12}CO $J = 2 - 1$. The gas temperature in the inner 4 au of the ProDiMo model is on the order of 500 K or more, which we do not see in our model, and none of our observations constrain gas temperatures at such small scales. ProDiMo specifically models the inner disk separately from the outer disk, and the temperature within this region is significantly warmer than the outer disk region.

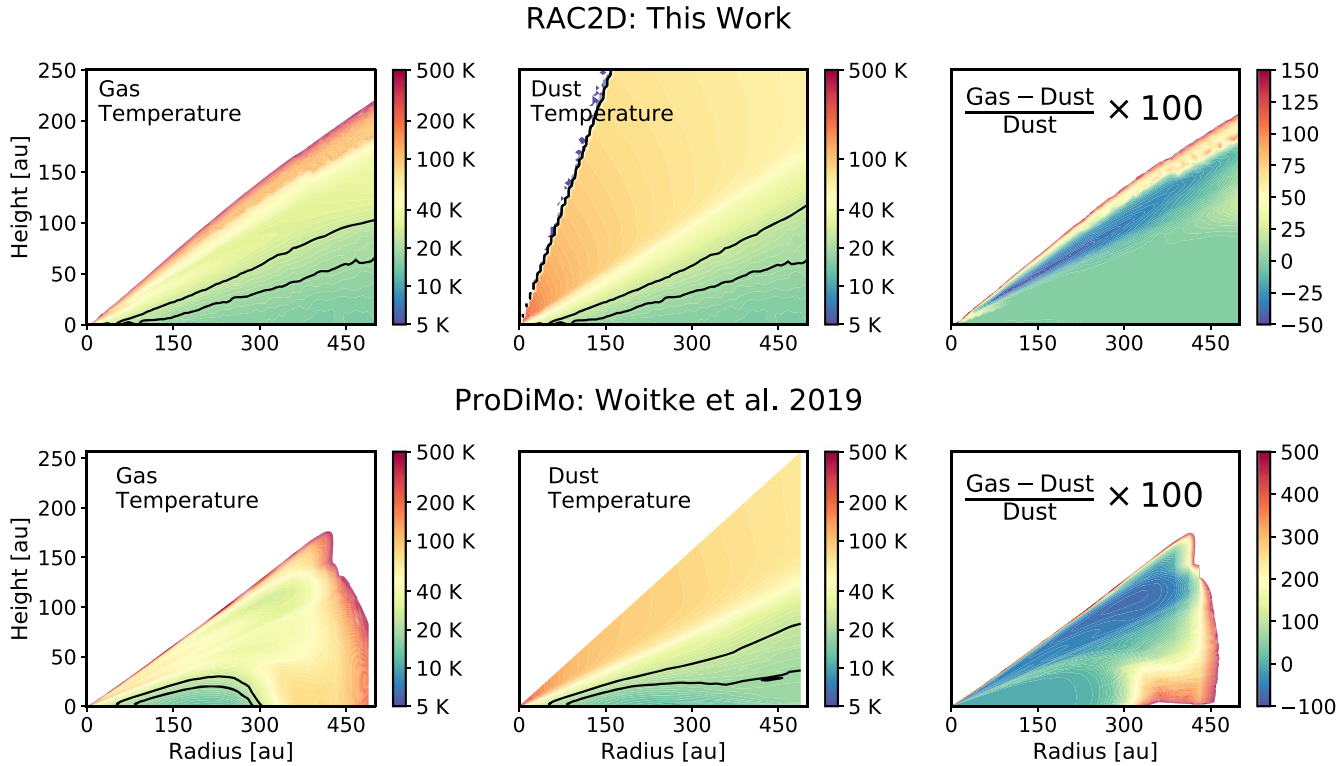

Figure B1. A comparison between this work's HD 163296 thermal structure that best reproduces the CO radial profiles, and the HD 163296 specific model from Woitke et al. (2019). The two contours in black follow 19 and 25 K.

Table B1
CO Upper Level Transitions

Transition	Model Flux Integrated Intensity (1×10^{-17} W m^{-2})	Observed Flux	Model in Observed Range?
5 − 4	0.504	1.04 ± 0.4	2σ
6 − 5	0.677	0.74 ± 0.29	1σ
7 − 6	0.807	0.9 ± 0.3	1σ
8 − 7	0.847	1.24 ± 0.55	1σ
9 − 8	0.766	0.91 ± 0.4	1σ
10 − 9	0.628	1.17 ± 0.35	2σ
11 − 10	0.566	1.13 ± 0.35	2σ
12 − 11	0.586	1.17 ± 0.35	2σ
13 − 12	0.606	1.52 ± 0.4	3σ
14 − 13	0.626	<1.6	True
15 − 14	0.648	1.03 ± 0.5	1σ
16 − 15	0.668	<1.3	True
17 − 16	0.680	0.75 ± 0.25	1σ
18 − 17	0.682	<0.9	True
19 − 18	0.671	<0.9	True
20 − 19	0.65	<0.9	True
21 − 20	0.621	<0.9	True
22 − 21	0.587	<0.9	True
23 − 22	0.549	<0.9	True

Note. Observed flux values are from Fedele et al. (2016) and references therein. Quoted errors are the 1σ noise measured in the continuum nearby to each line. The rightmost column shows whether the modeled flux agrees within 1σ, 2σ, or 3σ of the observation, or "True" if the modeled flux is below an upper limit.

ORCID iDs

Jenny K. Calahan https://orcid.org/0000-0002-0150-0125
Edwin A. Bergin https://orcid.org/0000-0003-4179-6394
Ke Zhang https://orcid.org/0000-0002-0661-7517
Kamber R. Schwarz https://orcid.org/0000-0002-6429-9457
Karin I. Öberg https://orcid.org/0000-0001-8798-1347
Viviana V. Guzmán https://orcid.org/0000-0003-4784-3040
Catherine Walsh https://orcid.org/0000-0001-6078-786X
Yuri Aikawa https://orcid.org/0000-0003-3283-6884
Felipe Alarcón https://orcid.org/0000-0002-2692-7862
Sean M. Andrews https://orcid.org/0000-0003-2253-2270
Jaehan Bae https://orcid.org/0000-0001-7258-770X
Jennifer B. Bergner https://orcid.org/0000-0002-8716-0482
Alice S. Booth https://orcid.org/0000-0003-2014-2121
Arthur D. Bosman https://orcid.org/0000-0003-4001-3589
Gianni Cataldi https://orcid.org/0000-0002-2700-9676
Ian Czekala https://orcid.org/0000-0002-1483-8811
Jane Huang https://orcid.org/0000-0001-6947-6072
John D. Ilee https://orcid.org/0000-0003-1008-1142
Charles J. Law https://orcid.org/0000-0003-1413-1776
Romane Le Gal https://orcid.org/0000-0003-1837-3772
Feng Long https://orcid.org/0000-0002-7607-719X
Ryan A. Loomis https://orcid.org/0000-0002-8932-1219
François Ménard https://orcid.org/0000-0002-1637-7393
Hideko Nomura https://orcid.org/0000-0002-7058-7682
Chunhua Qi https://orcid.org/0000-0001-8642-1786
Richard Teague https://orcid.org/0000-0003-1534-5186
Merel L. R. van't Hoff https://orcid.org/0000-0002-2555-9869
David J. Wilner https://orcid.org/0000-0003-1526-7587
Yoshihide Yamato https://orcid.org/0000-0003-4099-6941

References

Alarcón, F., Bosman, A. D., Bergin, E. A., et al. 2021, ApJS, 257, 8
Alarcón, F., Teague, R., Zhang, K., Bergin, E. A., & Barraza-Alfaro, M. 2020, ApJ, 905, 68
Andrews, S. M., Huang, J., Pérez, L. M., et al. 2018, ApJL, 869, L41
Astropy Collaboration, Price-Whelan, A. M., Sipőcz, B. M., et al. 2018, AJ, 156, 123
Bailer-Jones, C. A. L., Rybizki, J., Fouesneau, M., Mantelet, G., & Andrae, R. 2018, AJ, 156, 58
Benisty, M., Natta, A., Isella, A., et al. 2010, A&A, 511, A74
Bergin, E. A., Cleeves, L. I., Crockett, N., & Blake, G. A. 2014, FaDi, 168, 61
Bergin, E. A., Cleeves, L. I., Gorti, U., et al. 2013, Natur, 493, 644
Bergin, E. A., & Williams, J. P. 2017, in The Determination of Protoplanetary Disk Masses, ed. M. Pessah & O. Gressel (Cham: Springer), 1
Birnstiel, T., Dullemond, C. P., Zhu, Z., et al. 2018, ApJL, 869, L45
Boneberg, D. M., Panić, O., Haworth, T. J., Clarke, C. J., & Min, M. 2016, MNRAS, 461, 385
Booth, A. S., Walsh, C., Ilee, J. D., et al. 2019, ApJL, 882, L31
Bosman, A. D., Walsh, C., & van Dishoeck, E. F. 2018, A&A, 618, A182
Calahan, J., Bergin, E., Zhang, K., et al. 2021, ApJ, 908, 8
Cridland, A. J., Bosman, A. D., & van Dishoeck, E. F. 2020, A&A, 635, A68
Czekala, I., Loomis, R. A., Teague, R., et al. 2021, ApJS, 257, 2
D'Alessio, P., Calvet, N., & Woolum, D. S. 2005, in ASP Conf. Ser. 341, Chondrites and the Protoplanetary Disk, ed. A. N. Krot, E. R. D. Scott, & B. Reipurth (San Francisco, CA: ASP), 353
de Gregorio-Monsalvo, I., Ménard, F., Dent, W., et al. 2013, A&A, 557, A133
Dent, W. R. F., Pinte, C., Cortes, P. C., et al. 2019, MNRAS, 482, L29
Draine, B. T. 2003, ARA&A, 41, 241
Draine, B. T., & Li, A. 2001, ApJ, 551, 807
Du, F., & Bergin, E. A. 2014, ApJ, 792, 2
Dullemond, C. P., Juhasz, A., Pohl, A., et al. 2012, RADMC-3D: A multi-purpose radiative transfer tool, Astrophysics Source Code Library, ascl:1202.015
Facchini, S., Pinilla, P., van Dishoeck, E. F., & de Juan Ovelar, M. 2018, A&A, 612, A104
Fairlamb, J. R., Oudmaijer, R. D., Mendigutía, I., Ilee, J. D., & van den Ancker, M. E. 2015, MNRAS, 453, 976
Fedele, D., van Dishoeck, E. F., Kama, M., Bruderer, S., & Hogerheijde, M. R. 2016, A&A, 591, A95
Folsom, C. P., Bagnulo, S., Wade, G. A., et al. 2012, MNRAS, 422, 2072
Gaia Collaboration, Brown, A. G. A., Vallenari, A., et al. 2018, A&A, 616, A1
Garrod, R. T., Widicus Weaver, S. L., & Herbst, E. 2008, ApJ, 682, 283
Garufi, A., Quanz, S. P., Schmid, H. M., et al. 2014, A&A, 568, A40
Glassgold, A. E., Najita, J., & Igea, J. 2004, ApJ, 615, 972
Grady, C. A., Devine, D., Woodgate, B., et al. 2000, ApJ, 544, 895
Hayashi, C. 1981, PThPS, 70, 35
Henning, T., & Stognienko, R. 1996, A&A, 311, 291
Hunter, J. D. 2007, CSE, 9, 90
Isella, A., Huang, J., Andrews, S. M., et al. 2018, ApJL, 869, L49
Isella, A., Testi, L., Natta, A., et al. 2007, A&A, 469, 213
Jang-Condell, H. 2008, ApJ, 679, 797
Jorsater, S., & van Moorsel, G. A. 1995, AJ, 110, 2037
Kama, M., Bruderer, S., van Dishoeck, E. F., et al. 2016, A&A, 592, A83
Kama, M., Trapman, L., Fedele, D., et al. 2020, A&A, 634, A88
Kamp, I., & Dullemond, C. P. 2004, ApJ, 615, 991
Kamp, I., Tilling, I., Woitke, P., Thi, W. F., & Hogerheijde, M. 2010, A&A, 510, A18
Kanagawa, K. D., Muto, T., Tanaka, H., et al. 2015, ApJL, 806, L15
Kenyon, S. J., & Hartmann, L. 1987, ApJ, 323, 714
Law, C. J., Loomis, R. A., & Teague, R. 2021a, ApJS, 257, 3
Law, C. J., Teague, R., & Loomis, R. A. 2021b, ApJS, 257, 4
Li, A., & Draine, B. T. 2001, ApJ, 554, 778
Linsky, J. L. 1998, SSRv, 84, 285
Lynden-Bell, D., & Pringle, J. E. 1974, MNRAS, 168, 603
Mathis, J. S., Rumpl, W., & Nordsieck, K. H. 1977, ApJ, 217, 425
McClure, M. K., Bergin, E. A., Cleeves, L. I., et al. 2016, ApJ, 831, 167
McMullin, J. P., Waters, B., Schiebel, D., Young, W., & Golap, K. 2007, in ASP Conf. Ser. 376, Astronomical Data Analysis Software and Systems XVI, ed. R. A. Shaw, F. Hill, & D. J. Bell (San Francisco, CA: ASP), 127
Miotello, A., Bruderer, S., & van Dishoeck, E. F. 2014, A&A, 572, A96
Miotello, A., van Dishoeck, E. F., Kama, M., & Bruderer, S. 2016, A&A, 594, A85
Monnier, J. D., Harries, T. J., Aarnio, A., et al. 2017, ApJ, 838, 20
Muro-Arena, G. A., Dominik, C., Waters, L. B. F. M., et al. 2018, A&A, 614, A24

Najita, J. R., & Ádámkovics, M. 2017, ApJ, 847, 6
Nealon, R., Pinte, C., Alexander, R., Mentiplay, D., & Dipierro, G. 2019, MNRAS, 484, 4951
Öberg, K., Guzmán, V. V., Walsh, C., et al. 2021, ApJS, 257, 1
Öberg, K. I., & Bergin, E. A. 2016, ApJL, 831, L19
Öberg, K. I., Murray-Clay, R., & Bergin, E. A. 2011, ApJL, 743, L16
Okuzumi, S., Momose, M., Sirono, S.-i., Kobayashi, H., & Tanaka, H. 2016, ApJ, 821, 82
Penna, R. F., Sądowski, A., Kulkarni, A. K., & Narayan, R. 2013, MNRAS, 428, 2255
Pilbratt, G. L., Riedinger, J. R., Passvogel, T., et al. 2010, A&A, 518, L1
Pinte, C., Price, D. J., Ménard, F., et al. 2018a, ApJL, 860, L13
Pinte, C., Price, D. J., Ménard, F., et al. 2020, ApJL, 890, L9
Poglitsch, A., Waelkens, C., Geis, N., et al. 2010, A&A, 518, L2
Powell, D., Murray-Clay, R., Pérez, L. M., Schlichting, H. E., & Rosenthal, M. 2019, ApJ, 878, 116
Qi, C., D'Alessio, P., Öberg, K. I., et al. 2011, ApJ, 740, 84
Qi, C., Öberg, K. I., Andrews, S. M., et al. 2015, ApJ, 813, 128
Rab, C., Kamp, I., Dominik, C., et al. 2020, A&A, 642, A165
Rich, E. A., Wisniewski, J. P., Sitko, M. L., et al. 2020, ApJ, 902, 4
Rosenfeld, K. A., Andrews, S. M., Hughes, A. M., Wilner, D. J., & Qi, C. 2013, ApJ, 774, 16
Schoonenberg, D., & Ormel, C. W. 2017, A&A, 602, A21
Schwarz, K. R., Bergin, E. A., Cleeves, L. I., et al. 2018, ApJ, 856, 85
Seok, J. Y., & Li, A. 2017, ApJ, 835, 291
Shakura, N. I., & Sunyaev, R. A. 1973, A&A, 500, 33
Sloan, G. C., Kraemer, K. E., Price, S. D., & Shipman, R. F. 2003, ApJS, 147, 379
Stevenson, D. J., & Lunine, J. I. 1988, Icar, 75, 146
Teague, R. 2019, JOSS, 4, 1632
Teague, R., Bae, J., & Aikawa, Y. 2021, ApJS, 257, 18
Teague, R., Bae, J., & Bergin, E. A. 2019, Natur, 574, 378
Teague, R., & Foreman-Mackey, D. 2018, RNAAS, 2, 173
Tilling, I., Woitke, P., Meeus, G., et al. 2012, A&A, 538, A20
Trapman, L., Miotello, A., Kama, M., van Dishoeck, E. F., & Bruderer, S. 2017, A&A, 605, A69
van der Marel, N., van Dishoeck, E. F., Bruderer, S., et al. 2016, A&A, 585, A58
van der Marel, N., Williams, J. P., & Bruderer, S. 2018, ApJL, 867, L14
van't Hoff, M. L. R., Walsh, C., Kama, M., Facchini, S., & van Dishoeck, E. F. 2017, A&A, 599, A101
Virtanen, P., Gommers, R., Oliphant, T. E., et al. 2020, NatMe, 17, 261
Warren, S. G., & Brandt, R. E. 2008, JGRD, 113, D14220
Wichittanakom, C., Oudmaijer, R. D., Fairlamb, J. R., et al. 2020, MNRAS, 493, 234
Williams, J. P., & Best, W. M. J. 2014, ApJ, 788, 59
Williams, J. P., & McPartland, C. 2016, ApJ, 830, 32
Wilson, T. L. 1999, RPPh, 62, 143
Wisniewski, J. P., Clampin, M., Grady, C. A., et al. 2008, ApJ, 682, 548
Woitke, P., Kamp, I., Antonellini, S., et al. 2019, PASP, 131, 064301
Woitke, P., Kamp, I., & Thi, W. F. 2009, A&A, 501, 383
Woitke, P., Min, M., Pinte, C., et al. 2016, A&A, 586, A103
Woodall, J., Agúndez, M., Markwick-Kemper, A. J., & Millar, T. J. 2007, A&A, 466, 1197
Zhang, K., Booth, A. S., & Law, C. J. 2021, ApJ, 257, 5
Zhang, K., Blake, G. A., & Bergin, E. A. 2015, ApJL, 806, L7
Zhang, S., Zhu, Z., Huang, J., et al. 2018, ApJL, 869, L47